Atmospheric Environment 316 (2024) 120162

Contents lists available at ScienceDirect

Atmospheric Environment

journal homepage: www.elsevier.com/locate/atmosenv

Urban vertical air pollution gradient and dynamics investigated with low-cost sensors and large-eddy simulations

Louise B. Frederickson [a,b,e,*], Hugo S. Russell [a,b,e], Siegfried Raasch [g], Zhaoxi Zhang [a,b], Johan A. Schmidt [f], Matthew S. Johnson [d,e,f], Ole Hertel [c]

[a] Department of Environmental Science, Frederiksborgvej 399, Roskilde, DK-4000, Denmark
[b] Big Data Centre for Environment and Health (BERTHA), Aarhus University, Frederiksborgvej 399, Roskilde, DK-4000, Denmark
[c] Faculty of Technical Sciences, Aarhus University, Ny Munkegade 120, Aarhus, DK-8000, Denmark
[d] Department of Chemistry, University of Copenhagen, Universitetsparken 5, Copenhagen, DK 2100, Denmark
[e] AirScape, 88 Baker Street, London, W1U 6TQ, United Kingdom
[f] DevLabs, Nannasgade 28, Copenhagen, DK-2200, Denmark
[g] Institut für Meteorologie und Klimatologie, Leibniz Universität Hannover, Herrenhäuser Str. 2, Hannover, 30419, Germany

HIGHLIGHTS

- Investigation of pollution concentrations from street to urban background using low-cost sensors.
- A moderate correlation was found between traffic-related air pollution, noise, and traffic counts, influenced by wind speed and direction.
- No vertical gradient was detected with low-cost sensors, despite low sensor intervariability.
- Large-eddy simulation model runs using the PALM model system generally supported the measured observations.
- Vertical concentration profile is very sensitive to stratification.

GRAPHICAL ABSTRACT

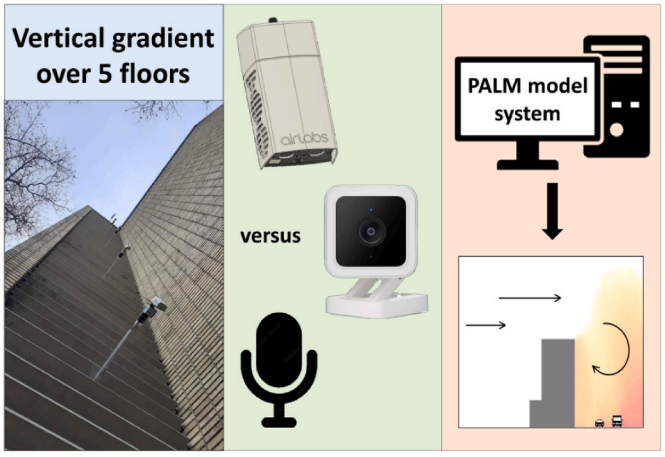

ARTICLE INFO

Keywords:
Low-cost sensors
Urban air pollution
TRAP
Vertical gradient
LES
PALM

ABSTRACT

A network of five low-cost air pollution sensor (LCS) nodes was deployed vertically on the exterior of the H. C. Ørsted Institute at the University of Copenhagen, Denmark, to investigate the transport of pollution from the road below. All LCS nodes measured $PM_{2.5}$, NO_2, and O_3 at 1-min time resolution, and one of them also measured noise. Traffic was monitored with a webcam, where traffic type and levels were derived using a machine-learning algorithm. We investigated how well traffic-related air pollution, noise, and real-time traffic counts serve as proxies for one another. The correlations between NO_2, noise, and traffic count exhibited relatively low values when considering all the data. However, these correlations significantly increased under southwesterly wind

* Corresponding author. Department of Environmental Science, Aarhus University, Frederiksborgvej 399, Roskilde, DK-4000, Denmark.
E-mail address: frederickson@envs.au.dk (L.B. Frederickson).

https://doi.org/10.1016/j.atmosenv.2023.120162
Received 18 August 2023; Received in revised form 16 October 2023; Accepted 17 October 2023
Available online 18 October 2023

direction and low wind speed, reaching $R^2 = 0.40$ for NO_2 and noise, $R^2 = 0.51$ for NO_2 and traffic volume, and $R^2 = 0.70$ for noise and traffic volume. These results indicate a common source, namely traffic, for all three parameters. The five LCS nodes spanning 25 m vertically had extremely low intervariability with minimum R^2-values of 0.98 for $PM_{2.5}$, 0.89 for NO_2, and 0.97 for O_3. The system could not detect a vertical gradient in pollution levels. Large-eddy simulation model runs using the PALM model system generally supported the lack of gradient observed in measured observations. Under slightly unstable stratification, concentration remained relatively constant with height for southwesterly and southerly winds. Conversely, winds from the north, west, and northwest showed an increase in concentration with height. For other wind directions, the concentration decreased with height by approximately 40 % to 50 %, which is not as strong as for neutral stratification, attributed to enhanced vertical mixing under unstable stratification. Based on the measurements and modeling, we conclude that the vertical concentration profile is very sensitive to stratification, and under these conditions, the concentration outside the window of a fifth-floor office is almost the same as for an office on the ground floor.

1. Introduction

Air pollution is a persistent and pressing problem in cities worldwide (Fowler et al., 2020). According to the United Nations, the proportion of the global population residing in urban areas exceeded 55 % in 2018, and this is projected to increase to 68 % by 2050, resulting in more densely populated regions with alarming levels of air pollution (United Nations, 2018). This pollution has negative impacts on society and individual human health, with particulate matter (PM) with an aerodynamic diameter smaller than 2.5 μm ($PM_{2.5}$), nitrogen dioxide (NO_2), and ozone (O_3) identified as leading causes of premature mortality and various respiratory and cardiovascular diseases (Curtis et al., 2006; Franklin et al., 2015; Zhang et al., 2018, 2019a). Air pollution is traditionally monitored using a sparse network of high-precision instruments for key gas pollutants and particulate matter, supplemented by modeling (Goodsite et al., 2021). More recently, high-density networks of small devices based on low-cost air pollution sensors (LCS) have emerged (Frederickson et al., 2022; Kang et al., 2022; Mead et al., 2013; Petäj et al., 2021). However, ground-based air pollution monitoring cannot describe the vertical structure of air pollution. This structure is therefore not typically accounted for in exposure assessments, which may lead to misclassification of exposures based on, for example, the elevation of an apartment or office (Wu et al., 2014). Vertical observations of air pollution can complement ground-based measurements to better characterize the three-dimensional structure of pollution (Hao et al., 2022).

In recent decades, there have been multiple studies of vertical profiles of air pollution. The most common methods include deployment of instruments at different heights on meteorological towers or multistorey buildings (Deng et al., 2015; Du et al., 2017; Fan et al., 2021; Harrison et al., 2012; Janhäll et al., 2003; Moreau-Guigon et al., 2007; Tevlin et al., 2017; Winderlich et al., 2014), balloons and aircraft carrying instruments (Li et al., 2015, 2018; Renard et al., 2020; Shi et al., 2022; Wang et al., 2020, 2021; Xing et al., 2017; Zhang et al., 2019b), instruments mounted in unmanned aerial vehicles (UAVs) (Chen et al., 2019; Li et al., 2018; Mamali et al., 2018; Shen et al., 2022; Song et al., 2021; Wang et al., 2020; Zheng et al., 2021), or accumulation in lichen (Pirintsos et al., 2006). For vertical measurements of particulate matter, the review by Dubey et al. (2022) gives an overview of the techniques and methods. Of these methods, manned aircraft and tethered balloons are expensive and only capture a snapshot in time. In contrast, towers or buildings provide semi-permanent installation space for instruments, and pollutants can be continuously measured across different heights.

Several studies have also investigated the differences in the vertical distribution of pollutants depending on street configuration, e.g. an open street, street canyon, or street canyon with viaduct (Chan and Kwok, 2000; Ezhilkumar et al., 2021; Ezhilkumar and Karthikeyan, 2020; Li et al., 2007; Micallef et al., 1998a; Pirintsos et al., 2006; Väkevä et al., 1999; Vardoulakis et al., 2002; Wong et al., 2019). Generally, the studies show how the dispersion and concentrations of air pollutants vary significantly depending on street configuration, prevailing wind direction, and wind speed as well as local sources. Multiple studies have also investigated the vertical profile of indoor air pollutants, for instance, while cooking (Micallef et al., 1998a, 1998b, 1999; Qiu et al., 2019; Zheng et al., 2022), or both the indoor and outdoor vertical profiles (Micallef et al., 1998c; Wong et al., 2019).

Higher-grade air pollution monitors for vertical measurements present several logistical challenges, whereas devices containing low-cost air pollution sensors have great potential, as they can be easily deployed with a high density over large areas, in both the horizontal and vertical directions. However, it is important to note that low-cost sensors have drawbacks and limitations relating to sensitivity, stability, and selectivity, which can vary depending on the type of low-cost sensor and even between sensors of the same type (Karagulian et al., 2019; Kumar et al., 2015; Morawska et al., 2018). Despite these shortcomings, low-cost sensors can still be extremely valuable since in many cases, it is not necessary to reach the same level of accuracy as for reference instruments, but instead to know the exact level of accuracy, and use the data from the sensors relative to each other (Nagendra et al., 2019; Wei et al., 2018). The level of accuracy is typically determined by comparing the low-cost sensor readings with data obtained from a regulatory air quality monitoring station (AQMS).

Only a limited number of studies have utilized low-cost sensors to establish vertical profiles of air pollution. For instance, Zheng et al. (2022) employed low-cost air pollution sensors to examine the vertical pollution levels of formaldehyde, carbon dioxide (CO_2), carbon monoxide (CO), total volatile organic carbon, methane, and three sizes of particulate matters (PM_1, $PM_{2.5}$, PM_{10}) in typical Chinese urban apartments that used a natural gas stove for cooking. Hao et al. (2022) measured the concentrations of nitric oxide (NO), NO_2, O_3, CO, $PM_{2.5}$, and PM_{10} at nine different heights on the Shanghai Tower (623 m) using low-cost sensor devices. In another study, Bao et al. (2020)employed a low-cost non-dispersive infrared CO_2 sensor on a tethered balloon to measure the vertical profile of CO_2 in the lower troposphere (0–1000 m) in southwestern Shijiazhuang, China. Schmitz et al. (2023) measured NO_2 and O_3 concentrations in three distinct street canyons located in Berlin, Germany, during the winter, spring, and summer seasons, but found no gradients within the sites.

In addition to air pollutants, noise has been identified as a significant contributor to the development and aggravation of various diseases (Hänninen et al., 2014). Numerous studies have explored the relationship between air and noise pollution, as well as the impact of environmental conditions on these pollutants and their correlations (Allen et al., 2009; Can et al., 2011; Forns et al., 2016; Kim et al., 2012; Klingberg et al., 2017; Ross et al., 2011; Shu et al., 2014; Tenailleau et al., 2016). There is evidence to suggest that both traffic-related air pollution and noise have adverse effects on cardiovascular health and that their joint impact may be even greater (Beelen et al., 2009; Gan et al., 2012). For example, research has shown that high noise levels can amplify the effects of traffic-related air pollution on heart rate variability in young healthy adults (Huang et al., 2013). It is important to consider noise measurements in order to gain a comprehensive understanding of multi-exposure situations at a specific location (Tenailleau et al., 2016). Traffic emits both noise and air pollutants simultaneously, meaning a strong correlation is expected. This relationship complicates health

impact assessments, and it becomes a potential confounder (Tétreault et al., 2013). Several studies have investigated the relationship between noise and air pollution, and their findings vary significantly (Allen et al., 2009; Fecht et al., 2016; Ross et al., 2011). Air pollutants directly related to traffic emissions, such as NO and NO_2, and black carbon, show stronger correlations compared to $PM_{2.5}$ and PM_{10}, while, there are significant variations between reported studies. Typically, the correlation is found to be highly influenced by factors such as time, location, weather conditions, and specific measurement parameters (Davies et al., 2009; Khan et al., 2020; Kheirbek et al., 2014; Kim et al., 2012). The emergence of multiple low cost alternatives to air pollution monitoring, microphones, and video cameras, necessitates an exploration of whether noise measurements and/or real-time traffic counts can serve as a proxy for pollution measurements using the latest low-cost technology.

Large-eddy simulation (LES) can be used to predict the transport and dispersion of pollutants in an urban environment (Kurppa et al., 2018; Xie and Castro, 2009). It explicitly calculates turbulent transport by the main energy containing turbulent eddies, while only the transport of small-scale eddies below the grid size of the model needs to be parameterized. The geometries of buildings within the simulation domain are typically well resolved by the numerical grid. The technique is particularly useful in simulating the complex flow patterns and turbulence that occur around buildings in urban environments. LES has been used to provide detailed information about the airflow and pollutant concentrations around buildings, which can then be used to optimize the design of buildings for improved ventilation and pollutant dispersion (Gronemeier and Sühring, 2019). Overall, the use of LES in studying airflow around buildings in polluted cities can contribute to improving air quality and public health in urban environments.

This study aims to determine the ability of low-cost sensors to measure the gradient in pollution between street and urban background in a specific street configuration. LCS nodes were vertically deployed on the exterior of the "C-building" at the H. C. Ørsted Institute (55.70094°N, 12.56151°W) of the University of Copenhagen, Denmark, to investigate the diffusion of pollution moving up from street level. Additionally, the study aims to establish links between traffic-related air pollution, noise levels, and real-time traffic counts, and investigate if one of these quantities can be used as a proxy for another with the low-cost equipment utilized.

2. Materials and methods

2.1. Campaign and site description

Five low-cost sensor nodes were installed on 2.5 m extruded aluminum masts affixed horizontally from each of the five floors of the H. C. Ørsted Institute's C-building, as seen in Fig. 1. With each floor being approximately 5 m high, the sensor nodes covered a vertical span of 25 m. The sensors were deployed from November 16, 2021, to February 24, 2022, for a total of 100 days, and then co-located for 1 month at a regulatory air quality monitoring station at H. C. Andersen's Boulevard for calibration.

The H. C. Ørsted Institute includes two six-story buildings (Building C and D) with flat roofs, as seen in Fig. 1. The road, Nørre Allé, runs directly in front of the H. C. Ørsted Institute from South to North. Nørre Allé has six lanes, two lanes for vehicles in each direction, two lanes for city buses through the center, and a bike and pedestrian path on either side of the road. A regulatory urban background air quality monitoring station (HCØ) is located on the roof of the D-building. The station measures NO_2 and O_3 by chemiluminescence and UV-absorption, respectively, with 30-min time resolution. Additionally, a gravimetric monitor is used for daily measurements of $PM_{2.5}$. A meteorological station also operates from the rooftop. During the campaign, south to southwesterly winds were prevalent, which means that the monitoring location was generally upwind of Nørre Allé. Prevalent wind directions and wind speeds are seen in Fig. 9 in the Appendix. Wind speeds ranged from 0.6 to 14.4 m s^{-1}, with an average of 4.8 m s^{-1}. The diurnal difference in wind data is not significant.

Approximately 3 km away from the H. C. Ørsted Institute is the regulatory air quality monitoring urban roadside station at H. C. Andersen's Boulevard (HCAB) in central Copenhagen. This station's measurements include NO_2, O_3, and $PM_{2.5}$, monitored by chemiluminescence, UV-absorption, and tapered element oscillating microbalance (TEOM) analyses, respectively, reported with 30-min time resolution, as well as daily gravimetric measurements of $PM_{2.5}$. Both HCAB and HCØ are operated under NOVANA (the Danish National Monitoring Program for Water and Nature) program (Ellermann et al., 2020). Note that the TEOM instrument is not accepted as a designated reference or field equivalent method (EPA, 2022), but is a higher-grade instrument that can be compared with LCS at a greater time resolution

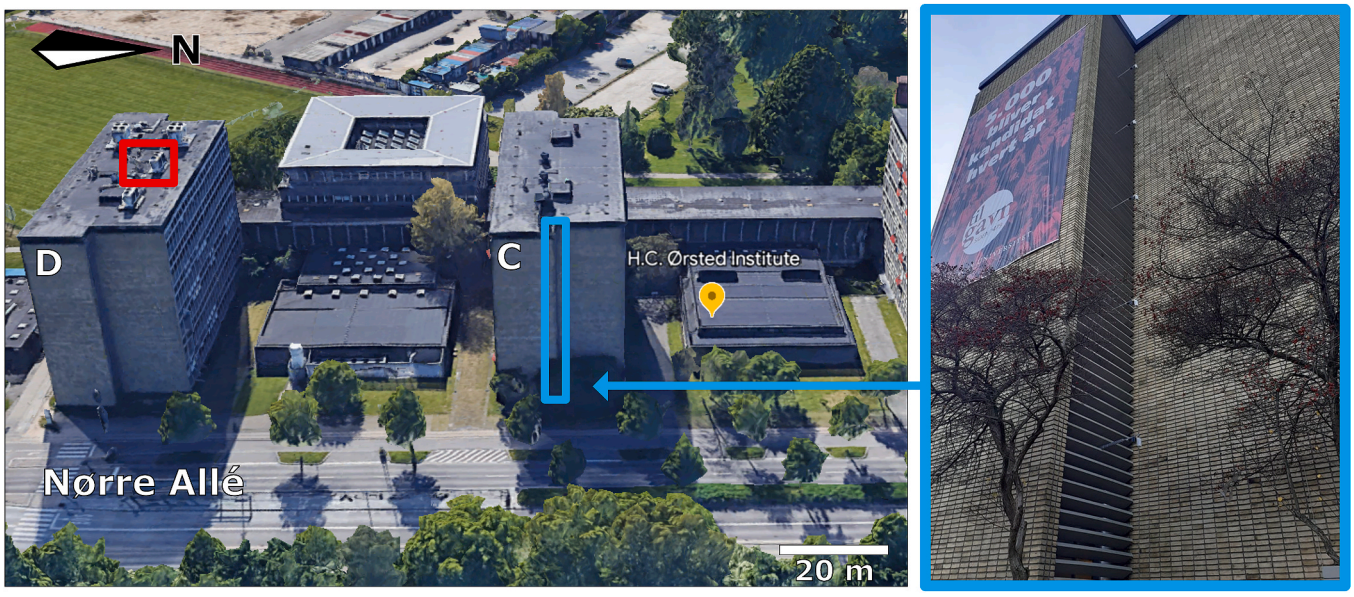

Fig. 1. Vertical deployment of the LCS nodes. On the left: Satellite image of the measurement site including the urban background air quality monitoring station (red box) on the rooftop of the D-building and the LCS node locations (blue box) on the C-building. On the right: Closer image of the five LCS nodes mounted to the C-building at H.C. Ørsted Institute. Satellite image from ©Google Maps (Google Maps, 2023).

than the gravimetric measurements.

2.2. Low-cost sensor nodes

Each floor of the C-building was outfitted with Gen5 nodes from DevLabs. The Gen5 nodes are low-cost, portable air quality monitoring devices encased in weatherproof housings (190 × 105 × 70 mm) allowing for full exposure to ambient air. The nodes are powered by USB cables and create a local network, allowing them to be connected to a WiFi network. This enables the transmission of raw data to a cloud database with a 1-min time resolution. The Gen5 nodes contain temperature and relative humidity sensors, electrochemical cells from Alphasense for measurement of NO_2 and O_3 (NO2–B43F and OX-B431, respectively), as well as an SPS30 sensor from Sensirion for $PM_{2.5}$ measurements (Bulot et al., 2020; Genikomsakis et al., 2018; Sensirion, 2020). The working principle and sensor specifications are described in detail elsewhere (Frederickson et al., 2023; Russell et al., 2022). Noise levels were recorded with a prototype noise sensor from DevLabs based on the GMI6027P–2C44DB microphone that measures sound from 63 to 10,000 Hz in separate wavelengths. The signal was analyzed using a ten-band spectrum analyzer. The average power in each band and the total power were recorded each minute. The noise sensor was placed on the second floor at the building's edge, alongside the extruded aluminum mast affixed to the floor.

2.3. Calibration and data analysis

The analyses were conducted in R version 4.1.2 (via *RStudio*) (R Core Team, 2017). Calibration of the LCS nodes was performed by co-locating the LCS nodes at HCAB for one month (February 24 to April 6, 2022). The LCS node readings are compared with the reference data, therefore the LCS node readings are aggregated to match the resolution of the reference readings. A multivariate linear regression model was applied to the co-location data for each LCS to obtain the individual calibration coefficients used to convert the raw sensor response to a concentration. This equation is applied for both NO_2 and O_3, where their cross-sensitivities to each other are corrected via a_3:

$$[X]_{\mathrm{Ref}} = a_0 + a_1 \mathrm{WE}_X + a_2 \mathrm{AE}_X + a_3 \mathrm{WE}_Y \quad (1)$$

Where $[X]_{\mathrm{Ref}}$ is the reference measurement of pollutant, X, in ppb, and when X is NO_2, Y is O_3 and vice versa. a_0 is the offset in ppb. WE_X and AE_X are the raw signals in V of the working and auxiliary electrodes, respectively, where a_1 and a_2 are their corresponding sensitivities in ppb V^{-1}. WE_Y is the raw signal in V of the working electrode of the cross-sensitive gas, and a_3 is its sensitivity in ppb V^{-1}. Temperature effects were minimized by the addition of a sun shield and the remaining effects were corrected using the auxiliary electrode.

For the prediction of $PM_{2.5}$, the sensor response, $\mathrm{SPS30\_PM_{2.5}}$, is used directly as input, together with the measured temperature (T) and relative humidity (RH):

$$[\mathrm{PM_{2.5}}]_{\mathrm{Ref}} = a_0 + a_1 \mathrm{SPS30\_PM_{2.5}} + a_2 T + a_3 RH \quad (2)$$

Where the offset (a_0), sensitivity (a_1), and correction coefficients (a_2 and a_3) are determined separately for each PM sensor.

To evaluate the performance of the multivariate linear model, the datasets were split into training (50 %) and validation (50 %) periods based on the dates. The model's performance was assessed using the coefficient of determination (R^2), slope, intercept, root-mean-square error (RMSE), mean bias error (MBE), and mean absolute error (MAE). Once the model's performance was established, we used the full co-location period to calibrate the sensors for the measurement campaign.

The non-parametric Wilcoxon–Mann–Whitney Rank test was used to perform statistical analysis and compare the differences among measured pollutant concentrations across different floors. Statistical significance was considered at the 5 % level ($p < 0.05$). Extremely small p-values are rounded down to 0.

To assess the influence of meteorological conditions on concentrations of NO_2, O_3, and $PM_{2.5}$ during the campaign, we employed generalized additive models (GAMs). These models were constructed using temperature, relative humidity, wind speed, wind direction, and irradiance as predictors for each LCS and reference instrument. The *gam()* function from the *mgcv* package in R was utilized for this purpose (Wood and Scheipl, 2020). The GAMs enabled us to quantify the extent to which variations in NO_2, O_3, and $PM_{2.5}$ concentrations were explained by these meteorological predictors. Additionally, we generated partial effects plots to visually understand the impact of each meteorological variable on pollutant concentrations across the entire measurement range.

2.4. Video analysis

Traffic count data was extracted from video footage recorded using a low-cost Wyze Cam V3 1080p video camera. This video camera was chosen because of its affordability, continuous recording capability, and high-resolution output. The camera was placed on the second floor at the building's edge, alongside the extruded aluminum mast affixed to the floor. Angled at approximately 45°, it provided clear visibility of the traffic lanes, as seen in Fig. 2. For vehicle counting, we employed an open-source object counting software called Ivy (Kajoh, 2022), which utilizes the 'You Only Look Once' (YOLOv3) object detection algorithm (Redmon and Farhadi, 2018). Implemented as a Python script, Ivy was capable of identifying and tracking vehicles as they moved through the monitored area based on visual patterns and features. The algorithm only counts vehicles that move through the blue counting lines and have a probability of above 0.75. The footage was categorized into *Up* and *Down* segments for the far and near road sections, respectively. An example of the analyzed video footage is presented in Fig. 2. In this depiction, the yellow box indicates the region of interest, while vertical blue lines denote separate counting lines for the two distinct road sections. The model was manually validated through twenty 1-min videos. During daylight hours, it exhibited an accuracy exceeding 90 % when compared to human counting. The model effectively differentiated between cars, buses, trucks, and motorbikes, accurately excluded bicycles from the count, and only counted parked vehicles once. However, the model's performance notably declined during twilight and nighttime (from 16:00 to 07:00), and therefore this data was not used.

2.5. PALM

The LES method is used to simulate the wind field and pollutant concentrations. In this study, the state-of-the-art, PALM model system, release 22.10,[1] is used, which was developed to simulate atmospheric and oceanic boundary layer flows on a wide range of spatial scales (Maronga et al., 2020). PALM solves the Navier-Stokes equations to determine the velocity field above and within the urban canopy. The pollutant transport and dispersion can be modeled via the Eulerian concentration transport equations. Equations are discretized by finite differences on a rectangular Cartesian grid. PALM has been successfully applied before to simulate urban environments including dispersion of air pollutants (e.g. Gronemeier and Sühring, 2019; Kurppa et al., 2018; Maronga et al., 2022) and it has been validated against wind tunnel (Gronemeier et al., 2021) and in-situ observations (Resler et al., 2021).

In our study, simulations with PALM have been carried out to explain the general shape of the observed vertical concentration profiles. For this reason, the model setup has been chosen to provide a qualitative comparison with the measurements. A quantitative comparison would have required including various boundary conditions in much more detail, e.g. to take into account the temporal change of meteorological

[1] https://gitlab.palm-model.org/releases/palm_model_system/-/releases/v22.10.

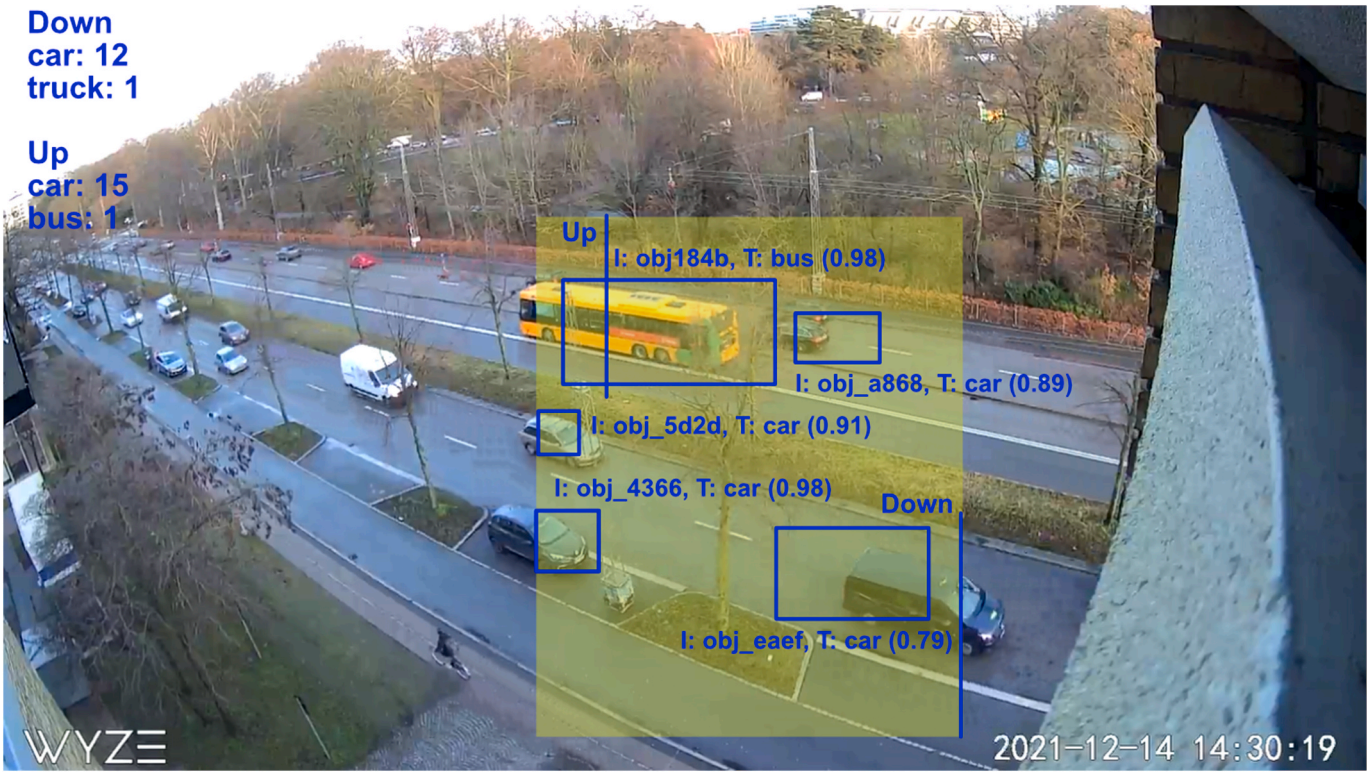

Fig. 2. Example frame from an analyzed video file. The frame shows the area of interest (yellow box), the *Up* and *Down* counting lines, a number of correctly identified cars, as well as a bus. The sum of counts for the current stage of the video are displayed in the top left corner.

conditions (daily cycle, and synoptic scale advection), effects from any kind of surface heterogeneity (caused by vegetation or thermal features of surfaces), or chemical reactions during the transport of emitted pollutants. Instead of exactly representing the conditions during the experiment, generic setups have been generated that well characterize typical conditions. The model domain has a size of 500 m along the horizontal directions and 1440 m vertically. An isotropic grid spacing of 1 m is used near the surface, in order to well resolve the turbulence near the building walls. Above a height of 100 m, the grid is vertically stretched to reduce the demand on computational resources. The buildings of the H. C. Ørsted Institute are represented as shown in Fig. 1. Topography, vegetation, and other surrounding buildings are disregarded since they would have only minor effects on the flow in the immediate vicinity of the H. C. Ørsted Institute. Simulations are driven by a geostrophic wind with a magnitude of 1 m s^{-1} in order to allow for larger timesteps, which reduces the computational time. Simulated mean concentration fields do not significantly depend on the magnitude of the geostrophic wind, as test runs with higher wind speeds have shown. The model is horizontally homogeneously initialized, with a vertical wind profile generated by a 1D-version of PALM. This profile represents the typical change of wind speed and direction with height in the atmospheric boundary layer (Ekman spiral) over a flat surface, and significantly helps to shorten the time until the 3D-simulation has reached a stationary state. A roughness length (z_0) of 0.1 m is used at the surface and building walls. A neutral or slightly unstable temperature stratification is assumed, which is more or less typical for wintertime conditions. The unstable stratification represents a surface sensible heat flux of about 10 W m^{-2}. During the simulation, along Nørre Allé, a passive tracer is emitted at the surface with a constant flux of 1 g m^{-2} s^{-1}. The absolute value of the flux is not of importance since for the analysis all concentrations are normalized by the simulated mean concentration that is observed directly above the street.

In order to determine the impact of wind direction on the results, eight runs for main wind directions W, SW, S, etc. have been carried out. Simulations are run for 7200 s. A stationary state is reached well before 3600 s, and model output is averaged over the last 3600 s of a run. This way turbulent fluctuations are almost filtered out.

3. Results

3.1. Calibration and intervariability

Results from co-locating a Gen5 node at HCAB are presented in Fig. 3. This figure illustrates the training and validation periods of the calibration model for NO_2, O_3, and $PM_{2.5}$. Evaluation statistics, along with the number of measurement points and measured ranges for the training and validation periods are provided in Tables 1 and 2 in the Appendix. For all pollutants, the concentration ranges were approximately the same for both the training and validation periods. It was determined that a time resolution of 30 min for the electrochemical cells and 2 h for the optical PM sensors yielded the most optimal calibration coefficients. During the validation period, the mean R^2 was 0.60 (0.02) for NO_2, 0.79 (0.01) for O_3, and 0.59 (0.01) for $PM_{2.5}$ with the respective standard deviations shown in parentheses. The slopes were less than 1 for all pollutants, with mean slopes of 0.8 (0.0), 0.9 (0.02), and 0.6 (0.01) for NO_2, O_3, and $PM_{2.5}$, respectively, indicating a slight underestimation of the concentrations. The sizes of RMSE, MBE, and MAE were similar for O_3 and $PM_{2.5}$, and slightly higher for NO_2, but still within acceptable limits. The intervariability between the LCS was consistently low for all pollutants, with the lowest R^2 being 0.89 for NO_2, 0.97 for O_3, and 0.98 for $PM_{2.5}$. This low intervariability makes the low-cost sensors highly suitable for relative measurements. These results are similar to, or better than, those reported in (Hong et al., 2021; Rogulski et al., 2022; Tryner et al., 2020).

Following deployment on the C-building, calibrated measurements from all Gen5 nodes were compared to reference readings obtained from the AQMS (HCØ), situated on the neighboring building's rooftop. The correlation matrices for each LCS on its respective floor compared to the

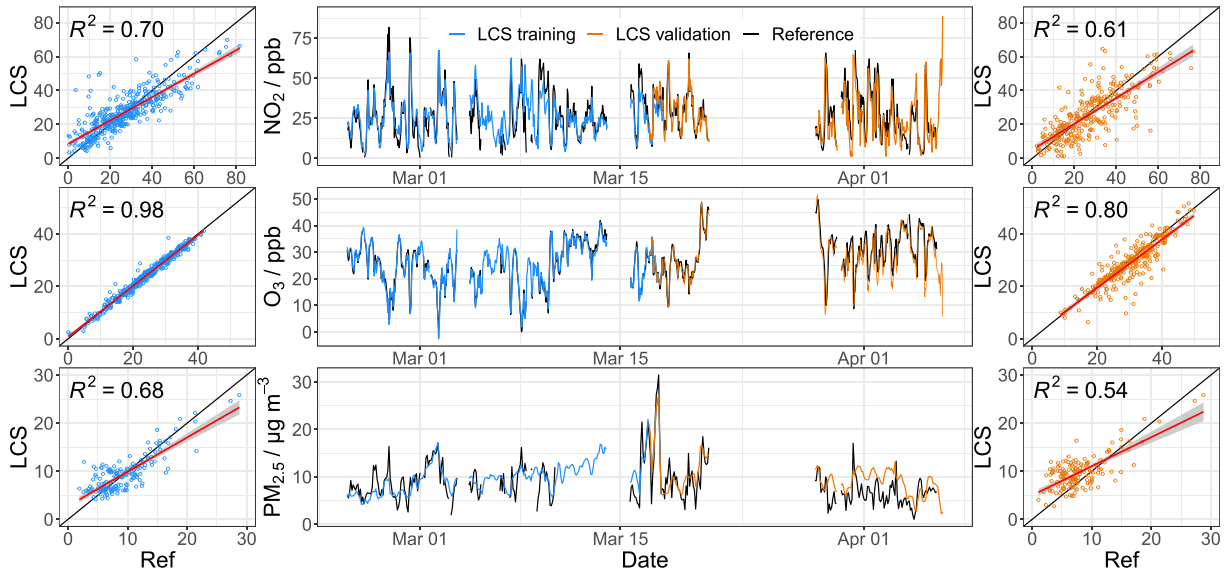

Fig. 3. Co-location measurements of one representative LCS node with reference (Ref) instruments at 30-min time resolution for NO_2 (top) and O_3 (middle), and 2-h time resolution for $PM_{2.5}$ (bottom). In the time series, the training (blue) and validation (orange) periods are shown together with their corresponding scatter plots. The scatter plots show the coefficient of determination between the reference and LCS measurements, a 1:1 line in black, and the regression line in red with its 95 % confidence interval as the grey shaded area.

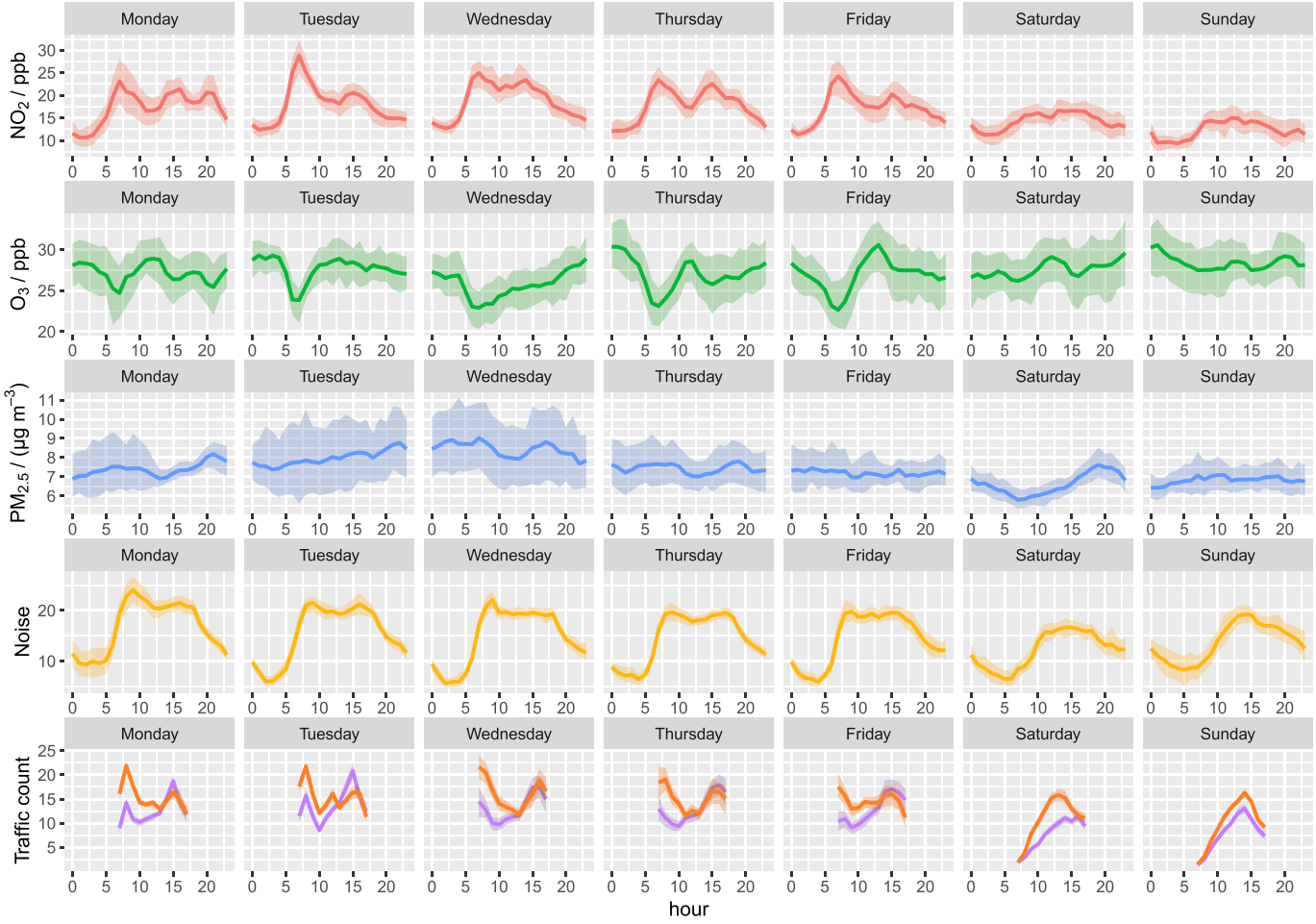

Fig. 4. Time variation of the concentration of NO_2, O_3 and $PM_{2.5}$, noise levels and traffic count from the first floor. The traffic count is split depending on which direction the traffic is driving, where purple represents *Up* and orange represents *Down*. All data is with a time resolution of 1 min.

reference instruments are presented in Figs. 10–12 in the Appendix. Compared with the reference readings from HCØ, the lowest R^2-values were 0.57 for NO_2, 0.91 for O_3, and 0.93 for $PM_{2.5}$ (compared with daily gravimetric measurements). The intervariability between the LCS was consistently low for all pollutants, despite being located on different floors, with the lowest R^2 being 0.78 for NO_2, 0.95 for O_3, and 0.99 for $PM_{2.5}$.

3.2. Air pollutants, noise, traffic count, and their associations

Time variation of the concentration of NO_2, O_3 and $PM_{2.5}$, noise levels and traffic count from the first floor is seen on Fig. 4. NO_2 concentrations exhibited distinct differences between weekdays and weekends, with higher levels observed on weekdays. During weekdays, substantial day-night gradients were observed, with an increase in the concentration of NO_2 from 4:00 to 5:00, followed by a decrease after 9:00. Additionally, in the late afternoon, there was an increase in NO_2 concentration. The NO_2 concentration was characterized by a bi-modal pattern akin to the two rush-hour periods. This increase occurred earlier on Wednesdays, with a less pronounced decrease in the afternoon. The morning rush-hour generally had higher NO_2 levels compared to the afternoon rush-hour period. On Mondays, an additional increase was seen around 20:00. Conversely, weekends displayed a slightly delayed rise in the morning, around 9:00, without an additional increase in the afternoon. During periods of elevated NO_2, the concentration of O_3 was found to be lowest, while weekends saw the highest O_3 levels. As for $PM_{2.5}$, no distinct daily patterns emerged; however, concentrations were consistently lower on weekends.

Similar patterns of weekday-weekend and day-night variations were observed in noise levels, with higher levels on weekdays. Substantial day-night gradients were evident, particularly on weekdays. There was a rise in noise levels during the early morning (around 5:00), followed by a decrease post 9:00, and a minor increase around 17:00. During weekends, the morning rise started later, around 9:00, and exhibited a more gradual decline throughout the night.

Traffic counts, recorded from 7:00 to 17:00, showed a higher volume of traffic heading "*Down*" (southward) toward central Copenhagen during the morning rush-hour. In the afternoon, traffic distribution became more balanced between directions. The lowest traffic counts were recorded during the weekend, with a steady increase from morning to early afternoon.

Moderate correlations were found among the pollutants. Specifically, a moderate inverse correlation was observed between NO_2 and O_3 ($R^2 = 0.47$), while the correlation between O_3 and $PM_{2.5}$ was more modest ($R^2 = 0.25$) and no correlation was seen between NO_2 and $PM_{2.5}$. Furthermore, there was no correlation between O_3, $PM_{2.5}$ and noise. The correlation between NO_2 and noise levels in the overall dataset yielded a relatively low R^2-value of 0.25. However, higher correlations are observed under specific wind speeds and directions, as seen in Fig. 13 in Appendix. A moderate NO_2-noise correlation ($R^2 = 0.40$) was found under southeasterly wind conditions, with wind speeds between 3 and 6 m s^{-1}. Similarly, a comparable correlation was observed at lower wind speeds (0–3 m s^{-1}) for wind directions from the NW, SE, and SW, with R^2-values ranging from 0.31 to 0.39. Conversely, no significant correlations between noise and NO_2 were observed at higher wind speeds ($\nu > 6$ m s^{-1}). Furthermore, the GAMs revealed that during southeasterly wind, noise levels explained 16 % of the variance in the NO_2 concentration. In contrast, for other wind directions, noise explained only 4 % to 7 % of the variance. Wind speed was a significant factor influencing the noise-NO_2 relationship. At low wind speeds ($\nu < 3$ m s^{-1}), noise levels explained 12.7 % of the variance in the overall dataset. This percentage decreased slightly to 11.9 % for wind speeds of 3–6 m s^{-1}, and dropped significantly to below 4 % for wind speeds exceeding 6 m s^{-1}, irrespective of wind direction.

No statistically significant relationships were observed between O_3, $PM_{2.5}$, and traffic count. The correlation between NO_2 and traffic count as well as the correlation between noise levels and traffic count in the entire dataset is relatively low, with R^2-values of 0.30 and 0.39, respectively. Nevertheless, a correlation was found between traffic volume and NO_2, similar to noise and NO_2, under specific wind direction and speed conditions. Specifically, under southwesterly winds and wind speeds of 0–3 m s^{-1}, the correlation of determination between NO_2 and traffic volume was 0.51. Similarly, a strong correlation with an R^2-value of 0.70 between traffic volume and noise was evident under the same conditions. Additionally, a correlation was noted between traffic volume and noise under southwesterly winds and higher speeds ($\nu = 3$–6 m s^{-1}), yielding an R^2-value of 0.52. For both cases, the coefficient of determination between noise and traffic volume would increase when only considering trucks in contrast to all vehicles. For example, for southwesterly winds and wind speeds between 0 and 3 m s^{-1}, the coefficient of determination between noise and traffic volume increased to 0.81 when considering only trucks and decreased to 0.60 when considering only cars.

3.3. Comparison between floors

The results from the measurement campaign indicated no significant vertical gradient in pollutant concentrations across the five floors. This observation is illustrated in Fig. 5 for NO_2, and corresponding figures for O_3 and $PM_{2.5}$ are presented in Figs. 14 and 15 in the Appendix. Generally, there was low variability between the sensors even when they were deployed on each floor. However, statistical analysis using the Wilcoxon–Mann–Whitney Rank test revealed significant differences among some measured concentrations at different floors, see Table 3 in the Appendix. The vertical profiles of the temperature and relative humidity, measured by the LCS at different floors, are shown in Fig. 20. Additionally, the temperature and relative humidity measured by the meteorological station on the rooftop are included. It can be seen that the temperature and relative humidity remain stable across all five floors. However, in general, the LCS nodes measure slightly higher temperatures and lower relative humidity compared to the meteorological station. This is due to the heating of the electric components within the nodes.

Figs. 16, 17, and 18 show partial effect plots of the GAMs for each meteorological variable affecting NO_2, O_3, and $PM_{2.5}$. These plots illustrate the non-linear impacts of meteorological variables across their observed range on the concentrations of NO_2, O_3, and $PM_{2.5}$. The meteorological variables account for 49.2 % to 53.5 % of the variance in NO_2 concentration, 65.6 % to 67.4 % for O_3, and 31.2 % to 31.7 % for $PM_{2.5}$. These results align with expectations and are consistent between LCS and reference measurements. Any unexplained variance is likely due to missing data on source emissions and activity. Partial effect plots of the GAMs for traffic count are shown in Fig. 19 in the Appendix. The traffic count is categorized into *Up* and *Down* for the three measured pollutants. There were no significant differences in the influence of traffic count on the LCS readings across different floors. Therefore, we only present partial plots for floor 2, as this is where the video camera is located. Note that traffic count has the highest influence on the NO_2 concentration (~10 %), followed by O_3 (~7 %) and $PM_{2.5}$ (~2 %), therefore the scales are different for the three pollutants. For NO_2 and O_3, only traffic counts at *Down* contribute to the variance explained in the LCS readings. Higher traffic counts at *Down* positively influence the NO_2 readings, while for O_3, the opposite is true, with higher traffic counts negatively affecting O_3 readings. As for the $PM_{2.5}$ readings, when considering the error bars, traffic count generally does not influence the LCS readings.

There is no significant difference between the amount of variance explained by the GAMs and the respective LCS floor location. Regarding NO_2, the most influential predictors are wind direction and wind speed, emphasizing the significance of dilution and transport processes. Higher concentrations of NO_2 are correlated with more stationary air parcels ($\nu < 3$ m s^{-1}), while lower concentrations are correlated with higher wind

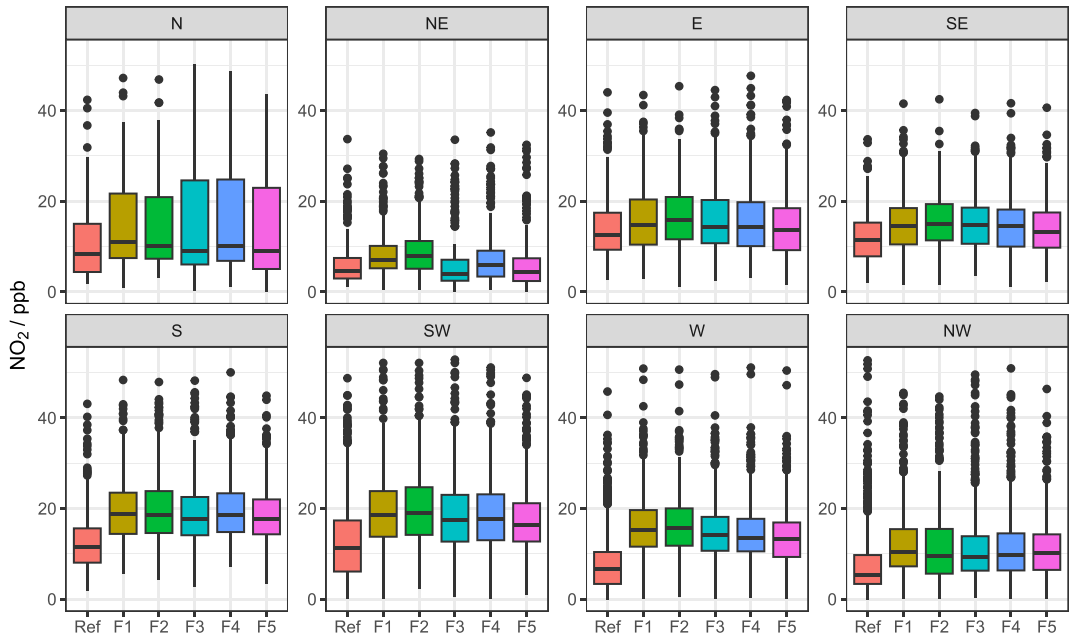

Fig. 5. Comparison of NO_2 concentrations measured with LCS nodes at the five floors (F*X* denotes floor number *X*) of the C-building, including results from the reference instruments placed at the rooftop of the D-building, across various wind direction bins.

speed values ($\nu > 3$ m s^{-1}). Some temperature effects on NO_2 concentrations are observed, particularly at lower temperatures ($T < 0$ °C).

For O_3, wind speed is the most important predictor. Higher concentrations of O_3 are linked to more moving air parcels ($\nu < 5$ m s^{-1}), whereas lower concentrations are correlated with reduced movement of air parcels ($\nu > 5$ m s^{-1}). This inverse relationship with NO_2 is expected since O_3 rapidly reacts with traffic-induced NO, forming NO_2. Wind direction explains the majority of the variance in LCS $PM_{2.5}$ measurements. No reference is added here since the only reference is based on daily gravimetric measurements, while the low-cost $PM_{2.5}$ sensors utilize optical measurements with a 1-min time resolution.

Our findings align with previous studies, highlighting wind speed as the primary meteorological factor influencing NO_2 levels (Carslaw et al., 2007; Elminir, 2007; Pearce et al., 2011). Compared to O_3, NO_2 exhibits less variance explained by meteorology, which accurately reflects the significant impact of local emissions and short-range transport on NO_x, as well as the role of photochemical production of O_3. The strong correlation with wind speed emphasizes the crucial role of dispersal and dilution in explaining local NO_2 concentrations from a meteorological perspective.

3.4. PALM results

The main purpose of the LES, which have been performed after the measurements were carried out, is to model the general behavior of the vertical concentration profiles as a function of wind speed and wind direction. Some typical examples from the eight wind directions that have been simulated for two stratifications (neutral and slightly unstable) will be presented. Fig. 6(a) shows streamlines of the near-surface flow at a height of 0.5 m around the H. C. Ørsted Institute for a case with neutral stratification and a background wind from the SW, which was the most prevalent wind direction during the experiment.

Due to the turning of wind direction to the left within the atmospheric boundary layer, the near-surface wind is oriented more south-southwest instead of southwest. Streamlines separate at the southwestern corner of the H. C. Ørsted Institute, and several recirculation zones appear along the eastern side of the building, where near-surface air is transported against the mean wind direction from the road east of the H. C. Ørsted Institute towards the building. Streamlines in a vertical cross section oriented along west-east at the sensor position (Fig. 6(b)) show that the air in the vicinity of the measurement system is transported directly from the surface up to the building top. The streamlines

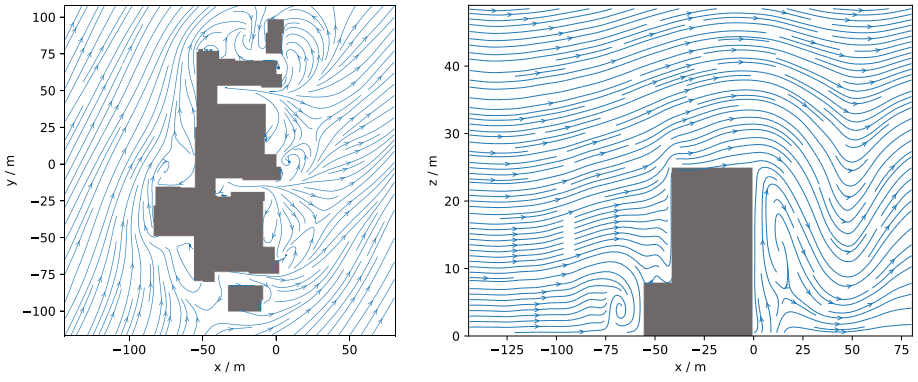

Fig. 6. Streamlines around the H. C. Ørsted Institute in (a) a horizontal cross section at 0.5 m height, and (b) a vertical cross section, for neutral stratification and a background wind from the SW. The origin of the coordinate system is centered at the monitoring array. Locations of buildings are represented by grey shaded areas.

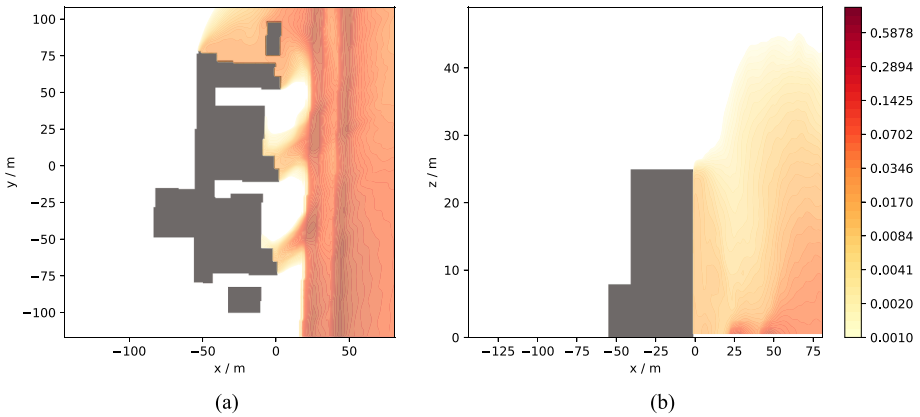

Fig. 7. Concentration of a passive scalar around the H. C. Ørsted Institute within (a) a horizontal cross section at 0.5 m height, and (b) a vertical cross section, for neutral stratification and a background wind from the SW. The scalar is normalized with the mean value directly above the street. The origin of the coordinate system is centered on the monitoring array. Locations of buildings are represented by grey shaded areas.

generally correspond with the flow field found around simple cubical-shaped obstacles, as found e.g. by Martinuzzi and Tropea (1993) from wind tunnel studies. The corresponding mean concentration field of a passive scalar that is released from the nearby road is displayed in Fig. 7, which shows cross sections at the same positions as for the streamlines.

While most of the scalar is advected eastward, away from the building, the horizontal cross section in Fig. 7(a) clearly shows a near-surface transport of scalar from the road, where maximum concentrations appear, towards the building within the recirculation zones, which is then transported upward along the wall up to the building top, as evident from Fig. 7(b).

The mean vertical concentration profile at the location of the measurement system is given in Fig. 8(a), together with the profiles obtained for the other simulated wind directions. In order to better visualize the change with height, concentrations for each of the profiles have been normalized with the concentration value at the lowest model grid point (0.5 m), respectively, so all profiles start at that point with a relative concentration of 1. For a background wind direction from the SW, the concentration is almost constant with height (fluctuations are probably due to insufficient time averaging), while for other directions a general decrease with height is observed. For wind directions from W and NW, concentrations decrease about 20 % to 30 % up to the fifth floor, while for the other wind directions, the decrease is about 70 % to 90 %. Above rooftop height, concentration values rapidly decrease to almost zero, which in turn implies that the rapid increase below the rooftop is an effect of the recirculation zone, which is strongest for wind directions from the W and NW. For slightly unstable stratification, as is typical for winter daytime conditions, the scalar is transported to greater heights due to better vertical turbulent mixing (see non-zero concentrations above roof level in Fig. 8(b)). Under such conditions, the concentration is still constant with height for a background wind from the SW, but also from the S, while for winds from the W and NW even a significant increase of concentration with height is observed. For other wind directions, the concentration decreases by about 40 % to 50 %, which is not as strong as for neutral stratification, due to the better vertical mixing under unstable stratification.

4. Discussion

The study aimed to establish links between traffic-related air pollution, noise levels, and real-time traffic levels with the low-cost equipment utilized. We utilized a video camera together with image detection to count traffic. Cameras offer a non-intrusive way to monitor traffic in contrast to other methods, such as pneumatic road tube counting, piezoelectric or magnetic sensors, or inductive loops (Ayaz et al., 2022), which are labor intensive, expensive to install, and require physical installations on the road. However, for our campaign, a separate detection model would need to be developed for vehicles with headlights switched on, in order to use the night-time data.

We found that wind direction and speed significantly modified

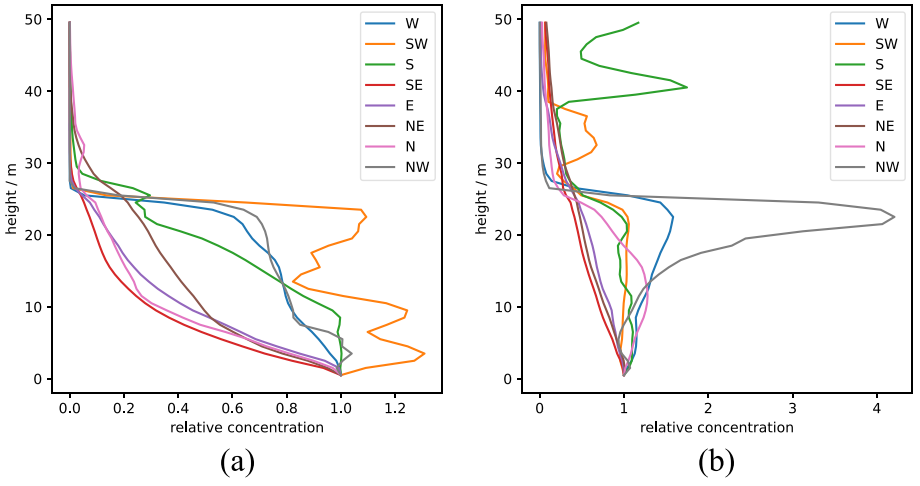

Fig. 8. Mean vertical profiles of passive scalar at the measurement location for the eight simulated wind directions, (a) for neutral stratification, and (b) for slightly unstable stratification. Note that the *y*-axis scale is expanded to 50 m, even though the rooftop height is approximately 25 m.

pollutant concentrations, noise levels, and the correlations between them. Our results showed a moderate correlation between NO_2 concentration, noise, and traffic counts under the conditions of southwesterly wind direction and low wind speed, suggesting that all three parameters have a common source, namely, traffic. Ross et al. (2011) found similar results, where they show how noise levels are temporally correlated with traffic and combustion pollutants and correlations are modified by the time of day, noise frequency, and wind. They found no correlation between NO_2 and noise when all hours were included, but NO_2 and noise were correlated when hours with high wind speeds were excluded.

The design of buildings can significantly affect both air and noise pollution levels, including factors such as building height, density, and material. Urban sound propagation is impacted by reflections from surfaces such as building facades and roofs, diffraction from edges, absorption, and scattering from irregular building surfaces. Environmental factors such as wind speed, wind direction, temperature, and temperature gradients can also greatly influence the correlation between air and noise pollution (King et al., 2016; Weber, 2009). Therefore, traffic noise may be confounded by atmospheric wind and, potentially, by distant noise. Sound travels faster in the direction of the wind and slower against it. Temperature gradients can also impact outdoor sound waves, for instance from road traffic, by refracting them towards or away from the ground (Khan et al., 2018).

The correlation between air and noise pollution and traffic is highly dependent on various conditions and factors. Previous studies have found strong relations between these parameters, while others have not found any correlation. This suggests that the relationship likely applies only to specific conditions. Therefore, noise levels could serve as an indicator of air pollution, but it requires careful parameterization and is applicable only in situations where precise determinations are not necessary. Consequently, it is crucial to measure local meteorological conditions such as temperature, wind speed, and wind direction, and to have a comprehensive understanding of the surrounding environment. For more accurate monitoring of air pollution, there is no substitute.

Another aim of the study was to assess the ability of low-cost sensors to measure pollution gradients between street level and urban background. The measurement campaign conducted at the H. C. Ørsted Institute building revealed no significant vertical gradient in pollutant concentrations across its five floors. However, according to PALM analysis, under neutral stratification, the relative concentration profiles for wind directions W and NW exhibited a decrease of approximately 20 % to 30 % up to the fifth floor, whereas, for other wind directions, the decrease was about 70 % to 90 %. In slightly unstable conditions, which are more realistic for the measurement campaign, the pollutants were transported to higher heights due to improved vertical turbulent mixing. Under such conditions, the concentration remained relatively constant with height for a background wind from the SW and S. However, for winds from the N, W, and NW, an increase in concentration with height was observed. For other wind directions, the concentration decreases by approximately 40 % to 50 %, which was not as pronounced as in neutral stratification, attributed to the enhanced vertical mixing under unstable stratification.

Overall, the simulations show a significant dependence of the vertical profile of concentration on the wind direction, which is to be expected since the building has a powerful impact on the near-surface flow field. It needs to be considered here, that the thermodynamic stability also affects the direction of the near-surface wind, so profiles for the same background wind direction but for different atmospheric stability may be hard to compare. Finally, we note that the wind sweeps evenly over the top of the building in all simulations showing that the rooftop is a good location for the 'urban background' monitoring station (at least under stable or slightly unstable stratification) as it is predicted to receive negligible contamination from local emissions from Nørre Allé. To further investigate the ability of the low-cost sensors to capture height-related pollution variations, we examined the *p*-values for each wind direction category, as presented in Tables 4, 5, and 6 in the Appendix. The results indicated that when LES simulations suggested the presence of a gradient between specific floors, the NO_2 sensor readings exhibited significant differences. Conversely, when LES simulations indicated no gradient in a particular wind direction bin, the NO_2 sensor readings did not show significant differences. For example, when considering the wind directions west and northwest, the *p*-values between most floors suggest significant differences in NO_2 concentration readings, consistent with the results from the LES simulations during slightly unstable stratification. In contrast, for the wind directions south and southwest, where LES simulations suggested almost constant concentration with height, the *p*-values from the floor comparisons indicate that NO_2 concentration is not significantly different between most floors. However, such relationships were not observed for O_3 or $PM_{2.5}$. It is important to note that while some sites may be statistically different from each other, there is no clear evidence of a vertical gradient in any of the pollutants across various heights. It should be noted that if more unstable conditions were considered, which might better simulate real-life scenarios, the gradients might become less distinct. The LCS nodes might accurately represent the air entering the building when windows are opened. Nonetheless, measured and modeled results of this study suggest that there is no substantial variation in concentration levels between working on the first floor and the fifth floor, for the building studied. The findings highlight the vertical concentration profile's sensitivity to stratification and the crucial role of location in determining air pollution gradients moving upward from a road. Generally, the dispersion and concentrations of air pollutants vary significantly depending on street configuration, prevailing wind direction, and wind speed as well as local sources. To obtain accurate assessments of pollutant gradients, measurement towers, which should be not affected by local circulations generated by nearby buildings or vegetation, are more suitable.

5. Conclusion

The combination of a video camera and machine learning algorithms was shown to be a very cost-effective method for automatically determining traffic volume and type. We found moderate correlations between traffic-related air pollution, noise, and traffic volume under specific conditions. During southwesterly winds and low wind speed, we observed significant correlations, with an R^2-value of 0.40 for NO_2 and noise, 0.51 for NO_2 and traffic volume, and 0.70 for noise and total traffic volume. This implies that noise levels and traffic counts can serve as indicators for air pollution, particularly in situations where a precise determination is not necessary. However, it is necessary to also measure local meteorological conditions, such as wind speed and direction, and for accurate monitoring of air pollution, there is no substitute.

This study found that the low-cost air pollution sensors were unable to detect a pollution gradient along the side of a 5-floor building (25 m), even though the low-cost sensors showed minimal sensor intervariability (R^2-values of 0.98 for $PM_{2.5}$, 0.89 for NO_2, and 0.97 for O_3). The pollution was enhanced relative to the urban background, with the excess pollution arising from the nearby road. LES simulations were used to corroborate the idea that air is swept vertically up the side of the building depending on wind direction from the roadway which would lead to as high pollution concentrations outside the window of a fifth-floor office, as for an office on the ground floor. The vertical concentration profile is very sensitive to stratification, but the model results in general support the measurement observations. Based on the low intervariability between the LCS nodes, LCS nodes can effectively indicate a vertical gradient in street configurations if there is a significant variation in air pollution with height. Vertical structure of air pollution in the urban environment is not typically accounted for in exposure assessments, which may lead to misclassification of exposures based on, for example, the elevation of an apartment or office, therefore wider adoption of vertical exposure measurements would improve exposure assessments and urban air pollution models.

CRediT authorship contribution statement

Louise B. Frederickson: Conceptualization, Methodology, Project administration, Formal analysis, Investigation, Validation, Visualization, Writing – original draft, preparation. **Hugo S. Russell:** Conceptualization, Methodology, Investigation, Formal analysis, Validation, Writing – review & editing. **Siegfried Raasch:** Investigation, Formal analysis, LES, PALM, Writing – original draft, preparation. **Zhaoxi Zhang:** Investigation, Formal analysis, Writing – review & editing. **Johan A. Schmidt:** Software, Resources, Supervision, Funding acquisition, Writing – review & editing. **Matthew S. Johnson:** Conceptualization, Methodology, Supervision, Funding acquisition, Writing – review & editing. **Ole Hertel:** Conceptualization, Methodology, Supervision, Funding acquisition, Writing – review & editing.

Declaration of competing interest

The authors declare the following financial interests/personal relationships which may be considered as potential competing interests:

Louise Bøge Frederickson reports a relationship with DevLabs/AirScape that includes: funding grants. Hugo Savill Russell reports a relationship with DevLabs/AirScape that includes: funding grants. Johan Albrecht Schmidt reports a relationship with DevLabs that includes: board membership, employment, and equity or stocks. Matthew Stanley Johnson reports a relationship with DevLabs/AirScape that includes: board membership, employment, and equity or stocks.

Data availability

Data will be made available on request.

Acknowledgement

The project was carried out as an activity under the Big Data Center for Environment and Health (BERTHA) supported by the Novo Nordisk Foundation. https://projects.au.dk/bertha/ (grant NNF17OC0027864). The authors acknowledge Jibran Khan for his help with generating the building geometries used for the PALM simulations. We also thank Sophia Pettitt-Kenney for helping with deploying the low-cost sensors node. All PALM simulations have been carried out on a cluster system of the Northern German Supercomputing Alliance (HLRN). We thank the students of the course *Atmospheric Environmental Chemistry* at the University of Copenhagen for their assistance in counting vehicles. We thank ACTRIS-DK for infrastructure used to support this work. We express our sincere gratitude to Christian Tortzen and Heino Theodor Langtoft for their assistance in allowing the study and installing the electronics for the low-cost sensor node deployment.

A. Appendix.

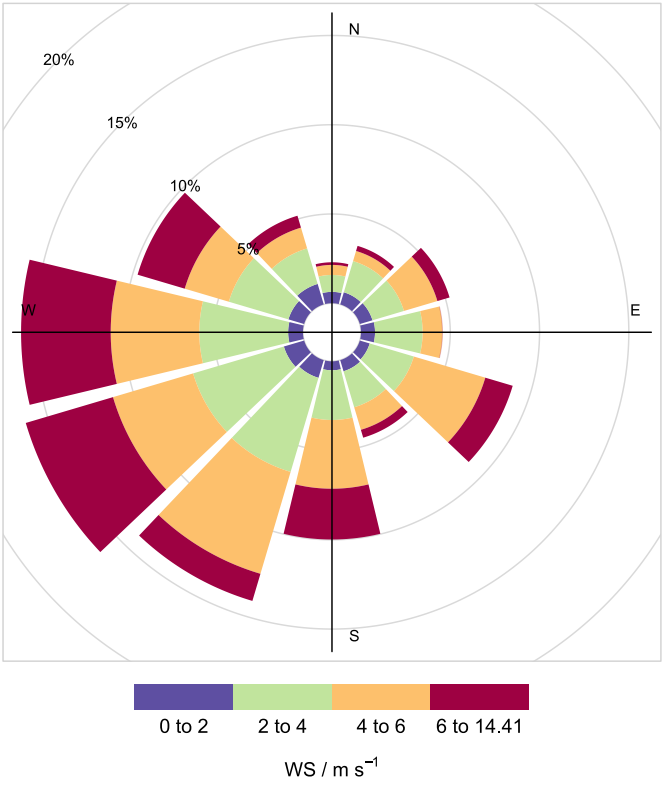

Fig. 9. Wind rose showing the wind directions and wind speeds during the campaign.

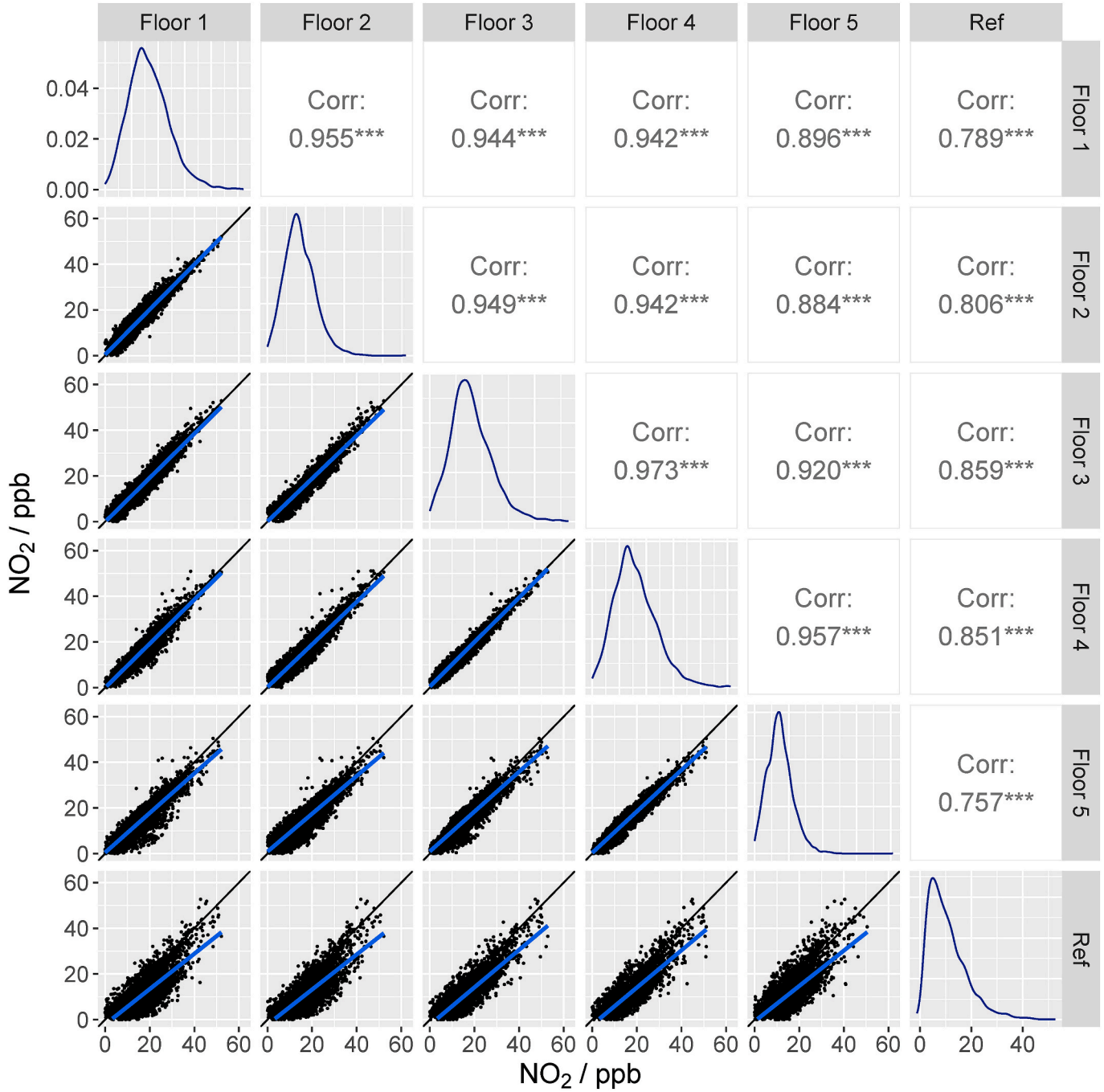

Fig. 10. Correlation matrix of the reference and the Gen5 nodes' calibrated NO_2 measurements with 30-min time resolution during the complete measurement period, displaying scatter plots (bottom left), density diagrams of distribution of data (diagonal), and pairwise Pearson's correlation coefficients (top right). Within the scatter plots are linear regression fit lines (blue), and a 1:1 line (black line). Note the different scales.

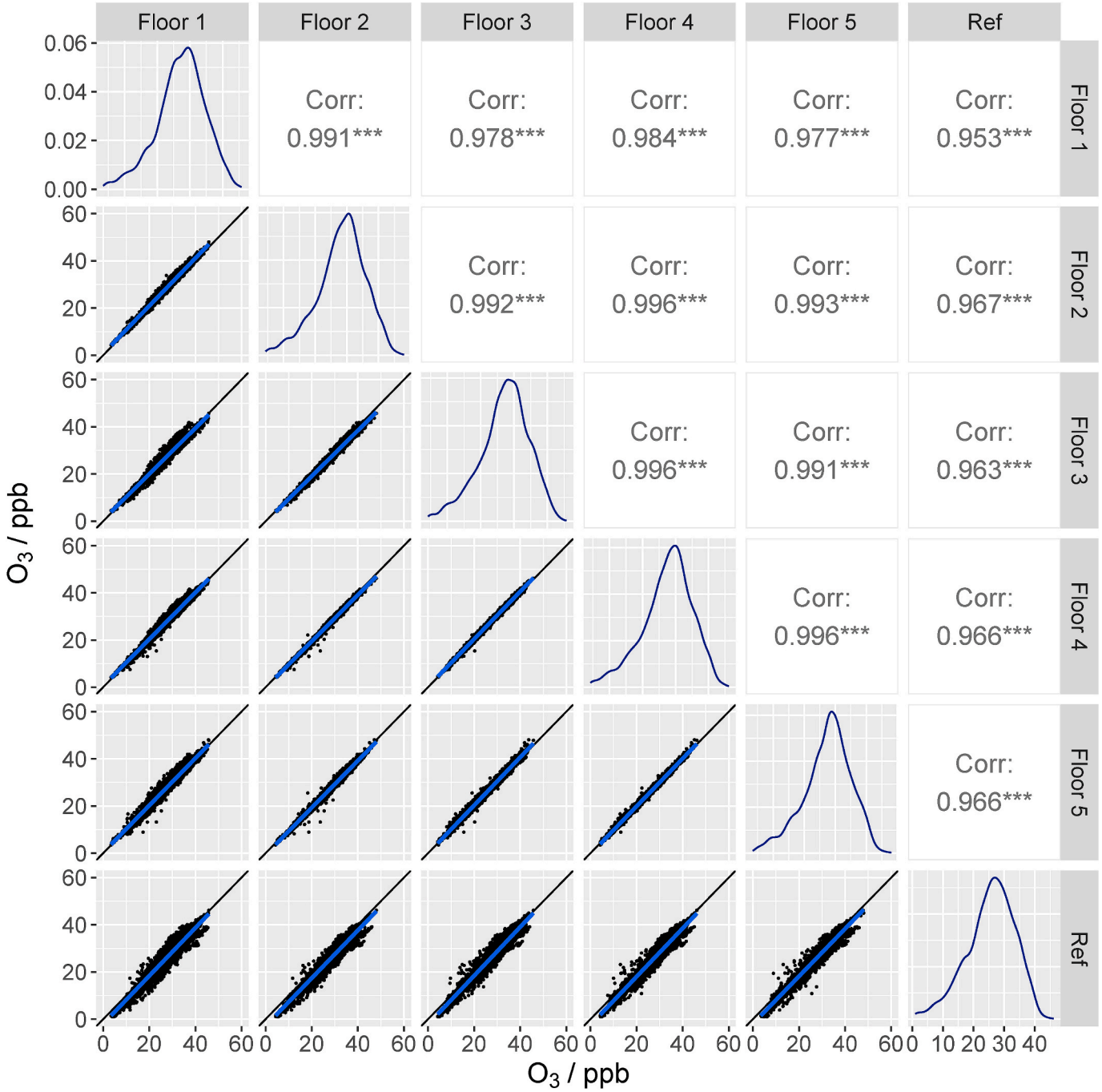

Fig. 11. Correlation matrix of the reference and the Gen5 nodes' calibrated O_3 measurements with 30-min time resolution during the complete measurement period, displaying scatter plots (bottom left), density diagrams of distribution of data (diagonal), and pairwise Pearson's correlation coefficients (top right). Within the scatter plots are linear regression fit lines (blue), and a 1:1 line (black line). Note the different scales.

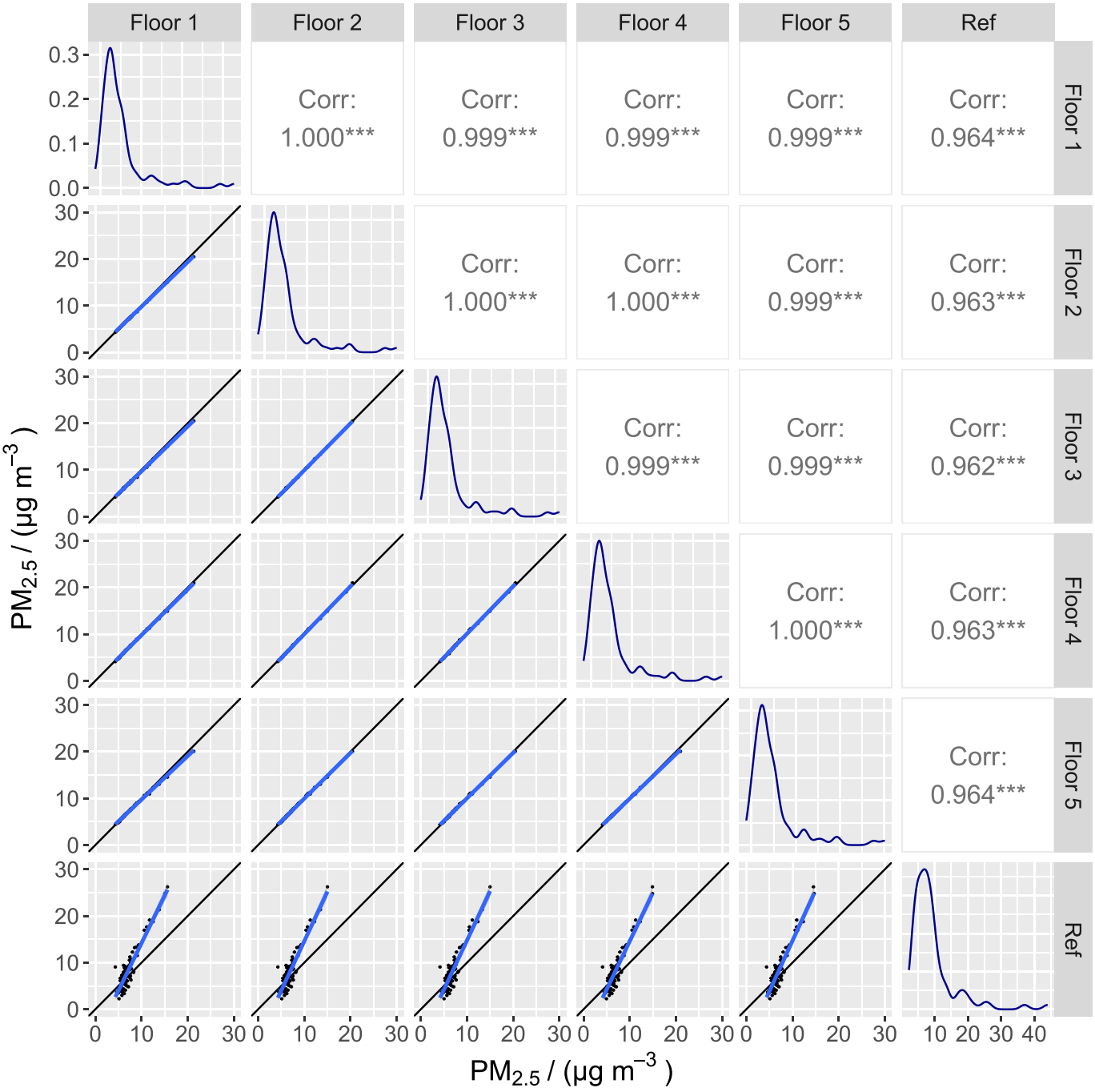

Fig. 12. Correlation matrix of the reference and the Gen5 nodes' calibrated $PM_{2.5}$ measurements with 24-h time resolution during the complete measurement period, displaying scatter plots (bottom left), density diagrams of distribution of data (diagonal), and pairwise Pearson's correlation coefficients (top right). Within the scatter plots are linear regression fit lines (blue), and a 1:1 line (black line). Note the different scales, and that the reference is a low volume sampler with a 1-day time resolution.

Table 1
Evaluation statistics for the training of the LCS nodes with the multivariate linear calibration model. The mean is an average over all nodes with their corresponding standard deviations (SD). The number of measurement points and reference instrument ranges during LCS node readings availability are also noted.

Pollutant	Sensor	R^2	Slope	Intercept	RMSE	MBE	MAE	Points	Range
NO_2	Gen5-282	0.69	0.69	8.3	6.9	0	6	354	0.3–81.7 ppb
	Gen5-283	0.66	0.66	9.2	7.1	0	6.3		
	Gen5-284	0.7	0.7	8.2	6.8	0	6		
	Gen5-285	0.7	0.7	8.2	6.8	0	5.9		
	Gen5-286	0.69	0.69	8.3	6.9	0	5.9		
	Mean	0.69	0.7	8.4	6.9	0	6		
	SD	0.02	0.02	0.44	0.09	0	0.13		
O_3	Gen5-282	0.98	0.98	0.6	1.3	0	0.9	354	0.09–41.8 ppb
	Gen5-283	0.98	0.98	0.5	1.2	0	0.9		
	Gen5-284	0.98	0.98	0.6	1.3	0	0.9		
	Gen5-285	0.98	0.98	0.5	1.2	0	0.9		
	Gen5-286	0.98	0.98	0.5	1.1	0	0.8		
	Mean	0.98	1	0.5	1.2	0	0.9		
	SD	0	0	0.05	0.06	0	0.06		
$PM_{2.5}$	Gen5-282	0.72	0.72	2.7	2.2	0	1.9	270	0.8–22.4 μg m^{-3}
	Gen5-283	0.73	0.73	2.6	2.1	0	1.9		
	Gen5-284	0.71	0.71	2.8	2.2	0	2		
	Gen5-285	0.71	0.71	2.8	2.2	0	2		
	Gen5-286	0.72	0.72	2.7	2.2	0	1.9		
	Mean	0.72	0.7	2.7	2.2	0	1.9		
	SD	0.01	0.01	0.08	0.02	0	0.03		

Table 2
Evaluation statistics for validation of the LCS nodes with the multivariate linear calibration model. The mean is an average over all nodes with their corresponding standard deviations (SD). The number of measurement points and reference instrument ranges during LCS node readings availability are also noted.

Pollutant	Sensor	R^2	Slope	Intercept	RMSE	MBE	MAE	Points	Range
NO_2	Gen5-282	0.6	0.76	5	9	−1.5	7.1	327	2.7–76.6 ppb
	Gen5-283	0.58	0.68	10.7	8.4	2.1	7.5		
	Gen5-284	0.64	0.8	5.1	8.7	−0.2	6.5		
	Gen5-285	0.6	0.77	5.2	9.1	−0.9	7		
	Gen5-286	0.6	0.76	6	9	−0.6	7.1		
	Mean	0.6	0.8	6.4	8.9	−0.2	7		
	SD	0.02	0	2.4	0.3	1.4	0.4		
O_3	Gen5-282	0.8	0.92	1	3.7	−1.3	2.6	328	8.8–49.8 ppb
	Gen5-283	0.78	0.88	1.4	3.7	−2.2	3.1		
	Gen5-284	0.8	0.95	0.9	3.8	−0.7	2.5		
	Gen5-285	0.78	0.92	1.2	3.9	−1.3	2.8		
	Gen5-286	0.79	0.92	1.3	3.8	−1.2	2.7		
	Mean	0.79	0.9	1.2	3.8	−1.3	2.8		
	SD	0.01	0.02	0.2	0.1	0.5	0.2		
$PM_{2.5}$	Gen5-282	0.6	0.63	4.9	2.4	1.8	2.8	328	0.3–33.4 μg m^{-3}
	Gen5-283	0.57	0.63	4.7	2.5	1.7	2.8		
	Gen5-284	0.58	0.61	4.9	2.4	1.8	2.9		
	Gen5-285	0.6	0.62	4.8	2.4	1.7	2.8		
	Gen5-286	0.58	0.62	4.8	2.5	1.8	2.9		
	Mean	0.59	0.6	4.8	2.4	1.8	2.8		
	SD	0.01	0.01	0.1	0.1	0.1	0		

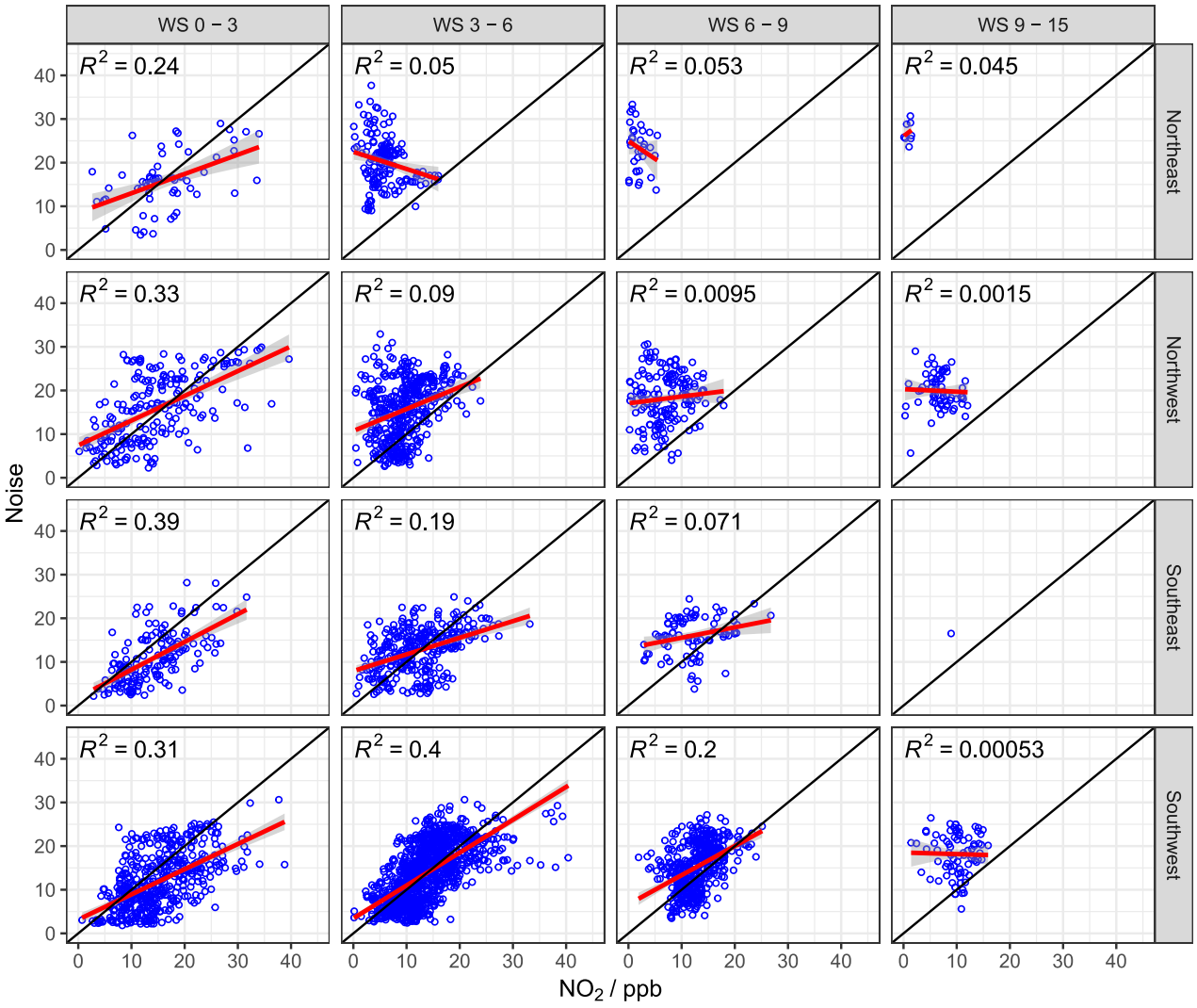

Fig. 13. Scatterplot of NO_2 vs. noise levels depending on wind direction and wind speed (WS). The correlation of determination between the NO_2 and noise levels for each scatterplot is shown, together with a 1:1 line in black, and the regression line in red with its 95 % confidence interval as the grey shaded area. Note that due to the limited availability of data within each wind direction bin, calculations were performed for only four wind direction ranges: 0–90° representing Northeast, 90–180° representing Southeast, 180–270° representing Southwest, and 270–360° representing Northwest.

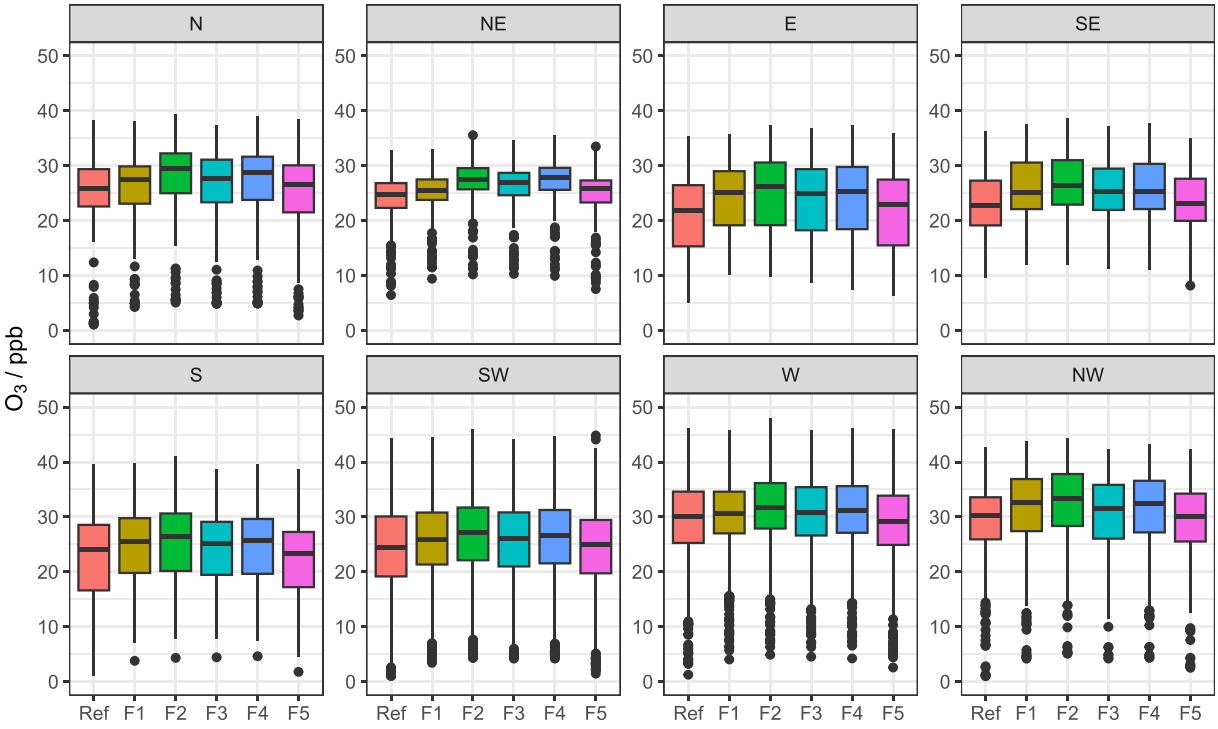

Fig. 14. Comparison of O_3 concentrations measured with LCS nodes at the five floors (F*X* denotes floor number *X*) of the C-building, including results from the reference instruments placed at the rooftop of the D-building, across various wind direction bins.

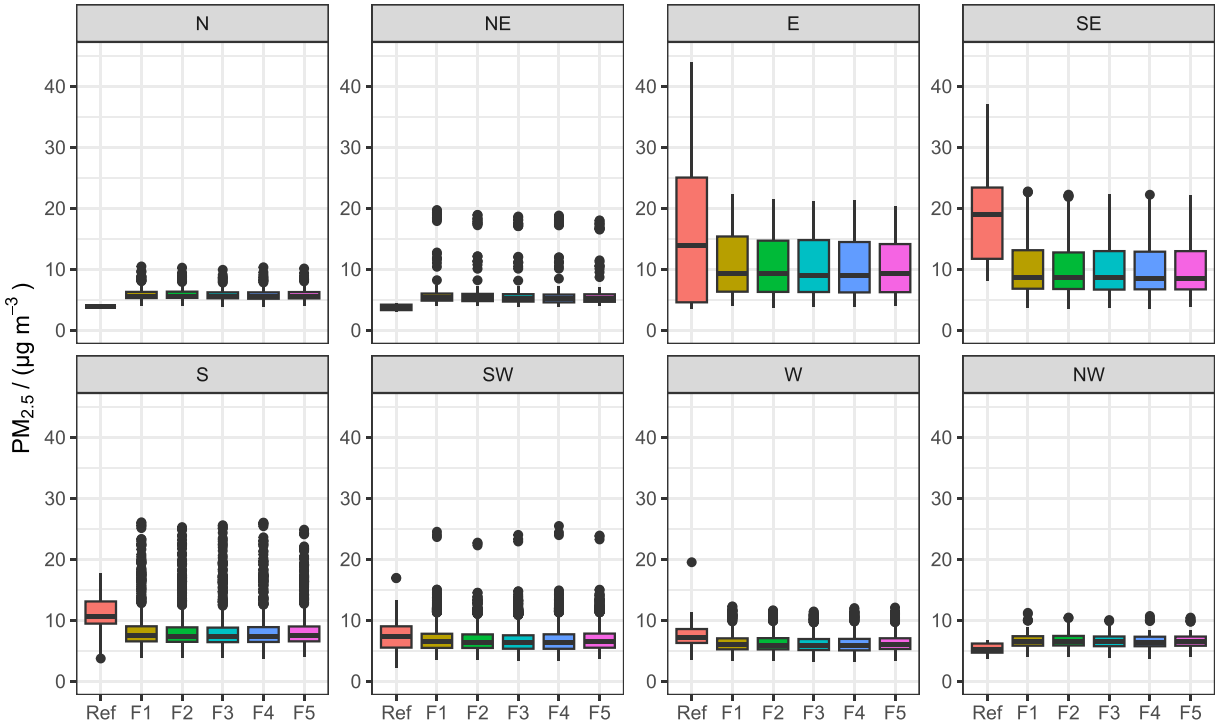

Fig. 15. Comparison of $PM_{2.5}$ concentrations measured with LCS nodes at the five floors (F*X* denotes floor number *X*) of the C-building, including results from the reference instruments placed at the rooftop of the D-building, across various wind direction bins. Note that the reference is a low volume sampler with a 1-day time resolution.

Table 3
Wilcoxon-Mann-Whitney U-tests of NO_2, O_3, and $PM_{2.5}$ concentrations at the five floors. Extremely small *p*-values are rounded down to 0. The *p*-values in bold are above 0.05. HCØ is the urban background reference station on the rooftop of the neighboring building.

NO_2	Floor 1	Floor 2	Floor 3	Floor 4	Floor 5
Floor 2	**0.098**				
Floor 3	0	0			
Floor 4	0	0	**0.5**		
Floor 5	0	0	0	0	
HCØ	0	0	0	0	0
O_3	Floor 1	Floor 2	Floor 3	Floor 4	Floor 5
Floor 2	0				
Floor 3	**0.45**	0			
Floor 4	0.018	0	0.0016		
Floor 5	0	0	0	0	
HCØ	0	0	0	0	**0.28**
$PM_{2.5}$	Floor 1	Floor 2	Floor 3	Floor 4	Floor 5
Floor 2	**0.37**				
Floor 3	0	0.004			
Floor 4	0	0.008	**0.89**		
Floor 5	**0.75**	**0.56**	0	0.0013	
HCØ	0.039	0.026	0.011	0.0128	0.032

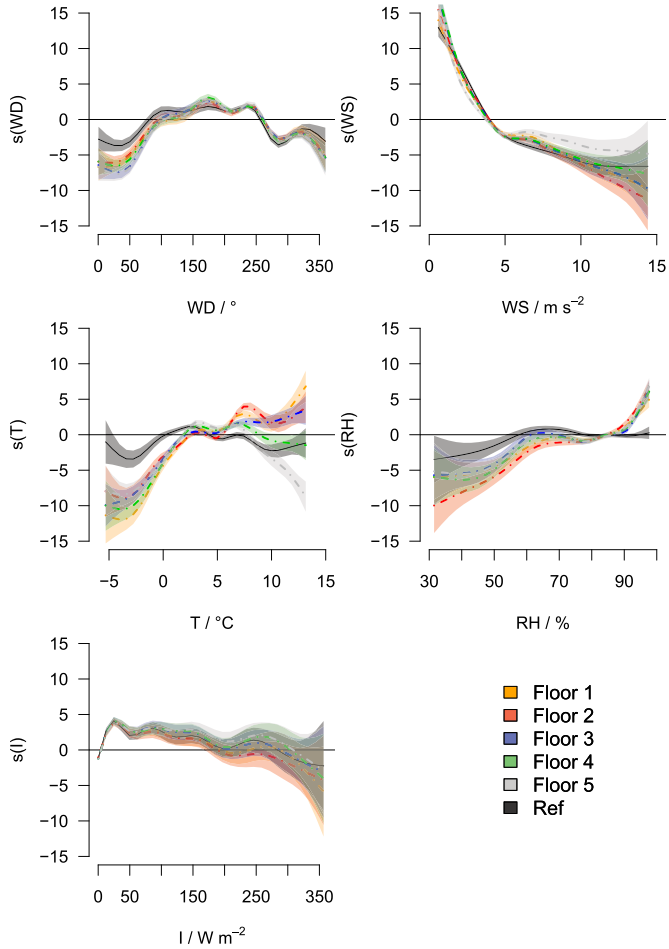

Fig. 16. Partial effects plots of each meteorological variable as calculated by the generalized additive models for NO_2 for each floor. The *y*-axes are in units of NO_2 concentration (ppb) but are labeled according to the smoothing functions applied by the GAM for each independent variable.

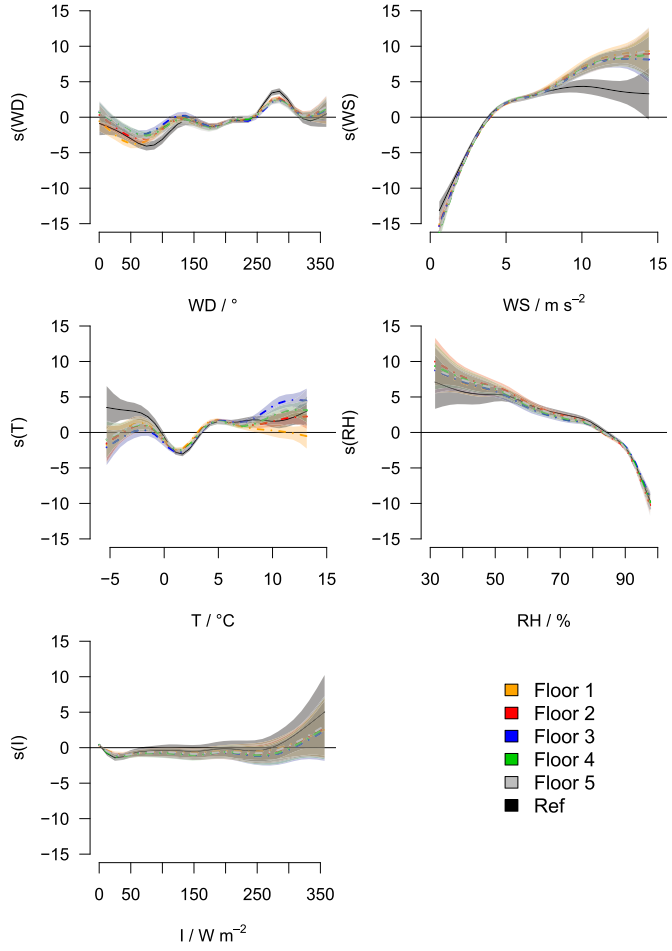

Fig. 17. Partial effects plots of each meteorological variable as calculated by the generalized additive models for O_3 for each floor. The *y*-axes are in units of O_3 concentration (ppb) but are labeled according to the smoothing functions applied by the GAM for each independent variable.

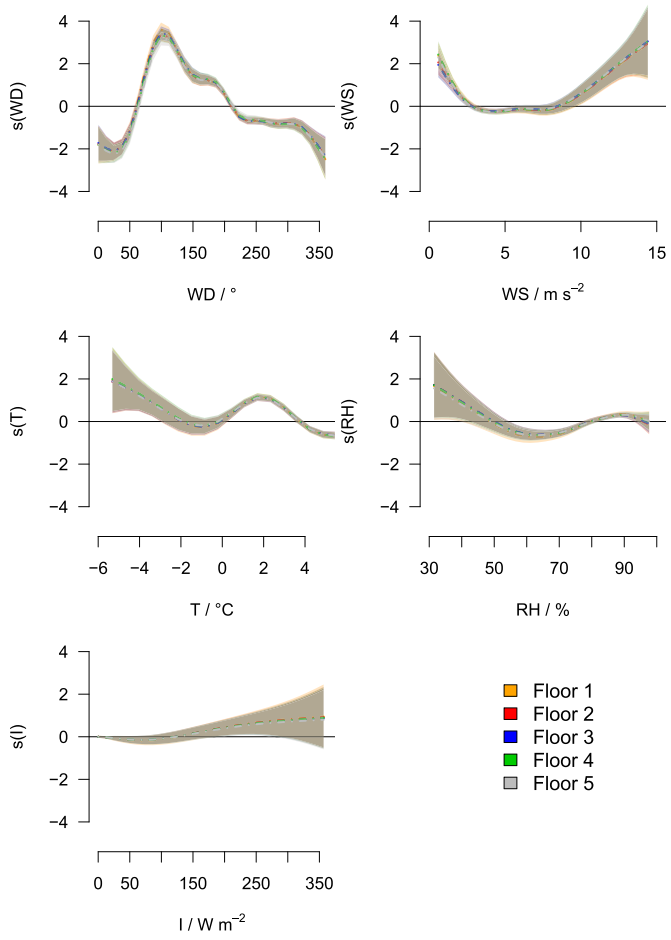

Fig. 18. Partial effects plots of each meteorological variable as calculated by the generalized additive models for $PM_{2.5}$ for each floor. The *y*-axes are in units of $PM_{2.5}$ concentration (μg m^{-3}) but are labeled according to the smoothing functions applied by the GAM for each independent variable.

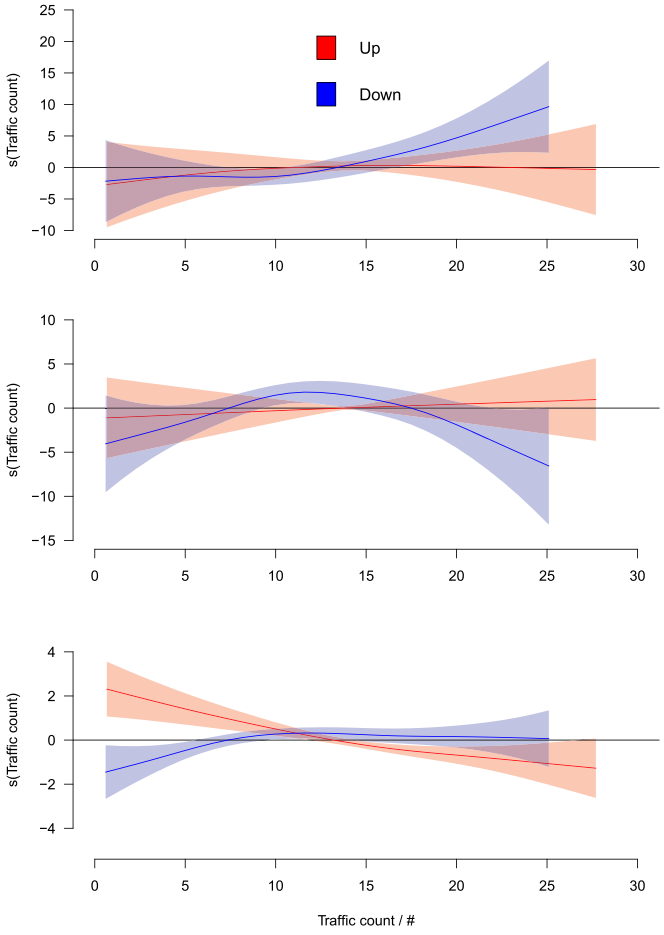

Fig. 19. Partial effects plots of traffic count, *Up* and *Down*, as calculated by the generalized additive models for NO_2 (top), O_3 (middle), and $PM_{2.5}$ (bottom) for floor 2. The *y*-axes are in units of the pollutant of interest (μg m^{-3} or ppb) but are labeled according to the smoothing functions applied by the GAM.

Table 4
Wilcoxon-Mann-Whitney U-tests of NO_2 concentrations at the five floors within each wind direction bin. Extremely small *p*-values are rounded down to 0. F*X* denotes floor number *X* and the *p*-values in bold are above 0.05. HCØ is the urban background reference station on the rooftop of the neighboring building.

	F1	F2	F3	F4	F5		F1	F2	F3	F4	F5
Northeast						**Southwest**					
F2	**0.26**					F2	0.01				
F3	0	0				F3	0.0069	**0.77**			
F4	0.0046	0	0			F4	**0.053**	**0.38**	**0.49**		
F5	0	0	**0.82**	0.001		F5	**0.061**	**0.38**	**0.45**	**0.97**	
HCØ	0	0	**0.092**	0.019	**0.18**	HCØ	0	0	0	0	0
East						**West**					
F2	**0.097**					F2	**0.37**				
F3	**0.79**	**0.13**				F3	0	0			
F4	**0.96**	**0.087**	**0.66**			F4	0	0	**0.16**		
F5	0.027	0	0.012	0.043		F5	0	0	0	0.0028	
HCØ	0.0026	0	0	0.0044	**0.48**	HCØ	0	0	0	0	0
Southeast						**Northwest**					
F2	**0.17**					F2	**0.13**				
F3	**0.38**	**0.55**				F3	0.0021	0			
F4	**0.77**	**0.26**	**0.53**			F4	0.0062	0	**0.7**		
F5	**0.059**	0	0.0048	0.032		F5	0	0	0.0015	0	
HCØ	0	0	0	0	0	HCØ	0	0	0	0	0
South						**North**					
F2	**0.76**					F2	**0.80**				
F3	0.024	0.013				F3	**0.44**	**0.32**			
F4	**0.97**	**0.77**	0.018			F4	**0.93**	**0.86**	**0.43**		
F5	0.0061	0.0032	**0.72**	0.0042		F5	**0.13**	**0.078**	**0.38**	**0.091**	
HCØ	0	0	0	0	0	HCØ	0.0054	0.002	0.0082	0.007	**0.38**

Table 5
Wilcoxon-Mann-Whitney U-tests of O_3 concentrations at the five floors within each wind direction bin. Extremely small *p*-values are rounded down to 0. F*X* denotes floor number *X* and the *p*-values in bold are above 0.05. HCØ is the urban background reference station on the rooftop of the neighboring building

	F1	F2	F3	F4	F5		F1	F2	F3	F4	F5
Northeast						**Southwest**					
F2	0					F2	0.0012				
F3	0	0.034				F3	**0.87**	0			
F4	0	**0.53**	0.0069			F4	**0.13**	**0.09**	**0.085**		
F5	**0.75**	0	0	0		F5	0	0	0	0	
HCØ	0.014	0	0	0	0.008	HCØ	0	0	0	0	**0.94**
East						**West**					
F2	**0.13**					F2	0				
F3	**0.74**	**0.052**				F3	**0.75**	0			
F4	**0.83**	**0.17**	**0.57**			F4	**0.073**	0.0074	**0.15**		
F5	0	0	0	0		F5	0	0	0	0	
HCØ	0	0	0	0	**0.085**	HCØ	0.004	0	0.0013	0	0.011
Southeast						**Northwest**					
F2	**0.052**					F2	0.029				
F3	**0.53**	0.01				F3	0.028	0			
F4	**0.99**	**0.057**	**0.48**			F4	**0.66**	0.0056	**0.066**		
F5	0	0	0	0		F5	0	0	0.0012	0	
HCØ	0	0	0	0	**0.41**	HCØ	0	0	0	0	0
South						**North**					
F2	**0.06**					F2	0.017				
F3	**0.23**	0.0024				F3	**0.64**	**0.056**			
F4	**0.71**	0.027	**0.39**			F4	**0.16**	**0.30**	**0.35**		
F5	0	0	0	0		F5	**0.55**	0.0035	**0.28**	0.048	
HCØ	0	0	0	0	**0.25**	HCØ	**0.19**	0	**0.080**	0.0077	**0.51**

Table 6
Wilcoxon-Mann-Whitney U-tests of $PM_{2.5}$ concentrations at the five floors within each wind direction bin. Extremely small *p*-values are rounded down to 0. F*X* denotes floor number *X* and the *p*-values in bold are above 0.05. HCØ is the urban background reference station on the rooftop of the neighboring building.

	F1	F2	F3	F4	F5		F1	F2	F3	F4	F5
Northeast						**Southwest**					
F2	**0.29**					F2	**0.52**				
F3	0.039	**0.27**				F3	0.014	**0.06**			
F4	0	0.012	**0.13**			F4	**0.075**	**0.23**	**0.51**		
F5	0.0079	**0.092**	**0.55**	**0.31**		F5	**0.49**	**0.18**	0.0017	0.015	
HCØ	0	0	0	0.0016	0	HCØ	**0.12**	**0.095**	**0.056**	**0.075**	**0.14**
East						**West**					
F2	**0.54**					F2	**0.7**				
F3	**0.44**	**0.87**				F3	0.0045	0.013			
F4	**0.32**	**0.67**	**0.78**			F4	0.0043	0.012	**0.93**		
F5	**0.31**	**0.61**	**0.73**	**0.95**		F5	**0.88**	**0.61**	0.0026	0.0028	
HCØ	**0.76**	**0.69**	**0.7**	**0.66**	**0.7**	HCØ	0.001	0.001	0	0	0.0014
Southeast						**Northwest**					
F2	**0.61**					F2	**0.76**				
F3	**0.58**	**0.99**				F3	**0.16**	**0.087**			
F4	**0.56**	**0.96**	**0.96**			F4	**0.068**	0.038	**0.65**		
F5	**0.64**	**0.95**	**0.92**	**0.9**		F5	**0.35**	**0.23**	**0.62**	**0.33**	
HCØ	0.015	0.01	0.01	0.012	0.012	HCØ	0.001	0.001	0.001	0.002	0.001
South						**North**					
F2	**0.44**					F2	**0.88**				
F3	**0.14**	**0.47**				F3	**0.43**	**0.33**			
F4	**0.32**	**0.81**	**0.63**			F4	**0.19**	**0.15**	**0.47**		
F5	**0.88**	**0.52**	**0.17**	**0.38**		F5	**0.57**	**0.45**	**0.87**	**0.41**	
HCØ	0.004	0.0035	0.003	0.0038	0.0041	HCØ	**0.089**	**0.089**	**0.095**	**0.10**	**0.089**

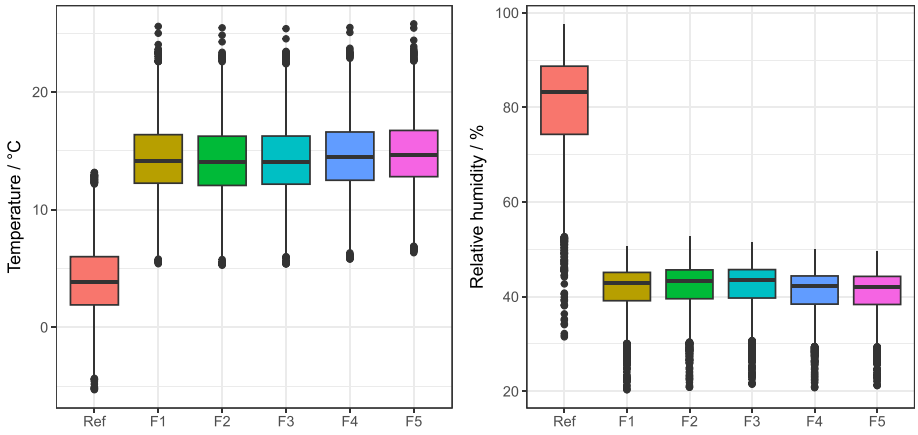

Fig. 20. Temperature (left) and relative humidity (right) measured internally by the LCS nodes on the five different floors with F*X* denoting the floor number.

References

Allen, R.W., Davies, H., Cohen, M.A., Mallach, G., Kaufman, J.D., Adar, S.D., 2009. The spatial relationship between traffic-generated air pollution and noise in 2 US cities. Environ. Res. 109 (3), 334–342.

Ayaz, S., Khattak, K.S., Khan, Z.H., Minallah, N., Khan, M.A., Khan, A.N., 2022. Sensing technologies for traffic flow characterization: From heterogeneous traffic perspective. J. Appl. Eng. Sci. 20 (1), 29–40.

Bao, Z., Han, P., Zeng, N., Liu, D., Cai, Q., Wang, Y., Tang, G., Zheng, K., Yao, B., 2020. Observation and modeling of vertical carbon dioxide distribution in a heavily polluted suburban environment. Atmos. Oceanic Sci. Lett. 13 (4), 371–379.

Beelen, R., Hoek, G., Houthuijs, D., van den Brandt, P.A., Goldbohm, R.A., Fischer, P., Schouten, L.J., Armstrong, B., Brunekreef, B., 2009. The joint association of air pollution and noise from road traffic with cardiovascular mortality in a cohort study. Occup. Environ. Med. 66 (4), 243–250.

Bulot, F.M.J., Russell, H.S., Rezaei, M., Johnson, M.S., Ossont, S.J.J., Morris, A.K.R., Basford, P.J., Easton, N.H.C., Foster, G.L., Loxham, M., Cox, S.J., 2020. Laboratory comparison of low-cost particulate matter sensors to measure transient events of pollution. Sensors 20 (8), 2219.

Can, A., Rademaker, M., Van Renterghem, T., Mishra, V., Van Poppel, M., Touhafi, A., Theunis, J., De Baets, B., Botteldooren, D., 2011. Correlation analysis of noise and ultrafine particle counts in a street canyon. Sci. Total Environ. 409 (3), 564–572.

Carslaw, D.C., Beevers, S.D., Tate, J.E., 2007. Modelling and assessing trends in traffic-related emissions using a generalised additive modelling approach. Atmos. Environ. 41 (26), 5289–5299.

Chan, L.Y., Kwok, W.S., 2000. Vertical dispersion of suspended particulates in urban area of Hong Kong. Atmos. Environ. 34 (26), 4403–4412.

Chen, Q., Wang, D., Li, X., Li, B., Song, R., He, H., Peng, Z., 2019. Vertical characteristics of winter ozone distribution within the boundary layer in Shanghai based on hexacopter unmanned aerial vehicle platform. Sustainability 11 (24), 7026.

Curtis, L., Rea, W., Smith-Willis, P., Fenyves, E., Pan, Y., 2006. Adverse health effects of outdoor air pollutants. Environ. Int. 32 (6), 815–830.

Davies, H.W., Vlaanderen, J.J., Henderson, S.B., Brauer, M., 2009. Correlation between co-exposures to noise and air pollution from traffic sources. Occup. Environ. Med. 66 (5), 347–350.

Deng, X., Li, F., Li, Y., Li, J., Huang, H., Liu, X., 2015. Vertical distribution characteristics of PM in the surface layer of Guangzhou. Particuology 20 (3–9).

Du, W., Zhao, J., Wang, Y., Zhang, Y., Wang, Q., Xu, W., Chen, C., Han, T., Zhang, F., Li, Z., Fu, P., Li, J., Wang, Z., Sun, Y., 2017. Simultaneous measurements of particle number size distributions at ground level and 260 m on a meteorological tower in urban Beijing, China. Atmos. Chem. Phys. 17 (11), 6797–6811.

Dubey, R., Patra, A., Allaudeen, N., 2022. Vertical profile of particulate matter: a review of techniques and methods. Air Quality, Atmosphere & Health 15 (6), 979–1010.

Ellermann, T., Nygaard, J., Nøjgaard, J.K., Nordstrøm, C., Brandt, J., Christensen, J., Ketzel, M., Massling, A., Bossi, R., Frohn, L.M., Geels, C., Jensen, S.S., 2020. The Danish Air Quality Monitoring Programme - Annual Summary for 2018. Technical Report No. 218. DCE – Danish Centre for Environment and Energy.

Elminir, H.K., 2007. Relative influence of air pollutants and weather conditions on solar radiation – Part 1: relationship of air pollutants with weather conditions. Meteorol. Atmos. Phys. 96 (3), 245–256.

EPA, 2022. List of Designated Reference and Equivalent Methods. https://www.epa.gov/system/files/documents/2022-06/designated_reference_and_equivalent_methods_-_06152022.pdf. (Accessed 6 December 2022).

Ezhilkumar, M.R., Karthikeyan, S., 2020. Vertical measurement of $PM_{2.5}$ and PM_{10} in street canyons and cohort health risk estimation at Chennai, south India. Environ. Eng. Sci. 37 (8), 535–547.

Ezhilkumar, M.R., Karthikeyan, S., Aswini, A.R., Hegde, P., 2021. Seasonal and vertical characteristics of particulate and elemental concentrations along diverse street canyons in South India. Environ. Sci. Pollut. Res. Int. 29 (57), 85883–85903.

Fan, S., Gao, C.Y., Wang, L., Yang, Y., Liu, Z., Hu, B., Wang, Y., Wang, J., Gao, Z., 2021. Elucidating roles of near-surface vertical layer structure in different stages of $PM_{2.5}$ pollution episodes over urban Beijing during 2004–2016. Atmos. Environ. 246, 118157.

Fecht, D., Hansell, A.L., Morley, D., Dajnak, D., Vienneau, D., Beevers, S., Toledano, M. B., Kelly, F.J., Anderson, H.R., Gulliver, J., 2016. Spatial and temporal associations of road traffic noise and air pollution in London: Implications for epidemiological studies. Environ. Int. 88, 235–242.

Forns, J., Dadvand, P., Foraster, M., Alvarez-Pedrerol, M., Rivas, I., López-Vicente, M., Suades-Gonzalas, E., Garica-Esteban, R., Esnaola, M., Cirach, M., Grellier, J., Basagaña, X., Querol, X., Guxens, M., Nieuwenhuijsen, M.J., Sunyer, J., 2016. Traffic-related air pollution, noise at school, and behavioral problems in Barcelona schoolchildren: A cross-sectional study. Environ. Health Perspect. 124 (4), 529–535.

Fowler, D., Brimblecombe, P., Burrows, J., Heal, M.R., Grennfelt, P., Stevenson, D.S., Jowett, A., Nemitz, E., Coyle, M., Liu, X., Chang, Y., Fuller, G.W., Sutton, M.A., Klimont, Z., Unsworth, M.H., Vieno, M., 2020. A chronology of global air quality. Phil. Trans. Math. Phys. Eng. Sci. 378 (2183), 20190314.

Franklin, B.A., Brook, R., Pope, C.A., 2015. Air pollution and cardiovascular disease. Curr. Probl. Cardiol. 40 (5), 207–238.

Frederickson, L.B., Sidaraviciute, R., Schmidt, J.A., Hertel, O., Johnson, M.S., 2022. Are dense networks of low-cost nodes better at monitoring air pollution? A case study in Staffordshire. Atmos. Chem. Phys. 22, 13949–13965.

Frederickson, L.B., Russell, H.S., Fessa, D., Khan, J., Schmidt, J.A., Johnson, M.S., Hertel, O., 2023. Hyperlocal air pollution in an urban environment – measured with low-cost sensors. Urban Clim. 52, 101684.

Gan, W.Q., Davies, H.W., Koehoorn, M., Brauer, M., 2012. Association of long-term exposure to community noise and traffic-related air pollution with coronary heart disease mortality. Am. J. Epidemiol. 175 (9), 898–906.

Genikomsakis, K.N., Galatoulas, N.-F., Dallas, P.I., Candanedo Ibarra, L.M., Margaritis, D., Ioakimidis, C.S., 2018. Development and on-field testing of low-cost portable system for monitoring $PM_{2.5}$ concentrations. Sensors 18, 1056–1072.

Goodsite, M.E., Hertel, O., Johnson, M.S., Jørgensen, N.R., 2021. Urban air quality: sources and concentrations. Air Pollution Sources, Statistics and Health Effects 193–214.

Google Maps, 2023. Satelite Image of H.C. Ørsted Institute.

Gronemeier, T., Sühring, M., 2019. On the effects of lateral openings on courtyard ventilation and pollution — a large-eddy simulation study. Atmosphere 10, 63.

Gronemeier, T., Surm, K., Harms, F., Leitl, B., Maronga, B., Raasch, S., 2021. Evaluation of the dynamic core of the palm model system 6.0 in a neutrally stratified urban environment: comparison between les and wind-tunnel experiments. Geosci. Model Dev. (GMD) 14, 3317–3333.

Hänninen, O., Knol, A.B., Jantunen, M., Lim, T.-A., Conrad, A., Rappolder, M., Carrer, P., Fanetti, A.-C., Kim, R., Buekers, J., Torfs, R., Iavarone, I., Classen, T., Hornberg, C., Mekel, O.C.L., 2014. Environmental burden of disease in Europe: Assessing nine risk factors in six countries. Environ. Health Perspect. 122 (5), 439–446.

Hao, X., Zhang, Y., Yu, G., He, B., Yang, F., Zou, Z., Zhang, C., Yang, X., Ouyang, B., Chang, Y., 2022. Online vertical measurement of air pollutants: development of a monitoring platform on a skyscraper and its application in Shanghai. Atmos. Pollut. Res. 13 (7), 101477.

Harrison, R., Dallósto, M., Beddows, D., Thorpe, A., Bloss, W., Allan, J., Coe, H., Dorsey, J., Gallagher, M., Martin, C., Whitehead, J., Williams, P., Langridge, J., Benton, A., Ball, S., Langford, B., Nicholas Hewitt, C., Davison, B., Smith, S., 2012. Atmospheric chemistry and physics in the atmosphere of a developed megacity (London): An overview of the REPARTEE experiment and its conclusions. Atmos. Chem. Phys. 12.

Hong, G.-H., Le, T.-C., Tu, J.-W., Wang, C., Chang, S.-C., Yu, J.-Y., Lin, G.-Y., Aggarwal, S. G., Tsai, C.-J., 2021. Long-term evaluation and calibration of three types of low cost $PM_{2.5}$ sensors at different air quality monitoring stations. J. Aerosol Sci. 157, 105829.

Huang, J., Deng, F., Wu, S., Lu, H., Hao, Y., Guo, X., 2013. The impacts of short-term exposure to noise and traffic-related air pollution on heart rate variability in young healthy adults. J. Expo. Sci. Environ. Epidemiol. 23 (5), 559–564.

Janhäll, S., Molnaŕ, P., Hallquist, M., 2003. Vertical distribution of air pollutants at the Gustavii Cathedral in Göteborg, Sweden. Atmos. Environ. 37 (2), 209–217.

Kajoh, N., 2022. Ivy. https://github.com/nicholaskajoh/ivy. Accessed: 2022-12-15.

Kang, Y., Aye, L., Ngo, T.D., Zhou, J., 2022. Performance evaluation of low-cost air quality sensors: a review. Sci. Total Environ. 818, 151769.

Karagulian, F., Barbiere, M., Kotsev, A., Spinelle, L., Gerboles, M., Lagler, F., Redon, N., Crunaire, S., Borowiak, A., 2019. Review of the performance of low-cost sensors for air quality monitoring. Atmosphere 10 (9), 506.

Khan, J., Ketzel, M., Kakosimos, K., Sørensen, M., Jensen, S.S., 2018. Road traffic air and noise pollution exposure assessment – a review of tools and techniques. Sci. Total Environ. 634, 661–676.

Khan, J., Kakosimos, K., Jensen, S.S., Hertel, O., Sørensen, M., Gulliver, J., Ketzel, M., 2020. The spatial relationship between traffic-related air pollution and noise in two Danish cities: Implications for health-related studies. Sci. Total Environ. 726, 138577.

Kheirbek, I., Ito, K., Neitzel, R., Kim, J., Johnson, S., Ross, Z., Eisl, H., Matte, T., 2014. Spatial variation in environmental noise and air pollution in New York city. J. Urban Health 91 (3), 415–431.

Kim, K.-H., Ho, D.X., Brown, R.J.C., Oh, J.M., Park, C.G., Ryu, I.C., 2012. Some insights into the relationship between urban air pollution and noise levels. Sci. Total Environ. 424, 271–279.

King, E.A., Bourdeau, E.P., Zheng, X.Y.K., Pilla, F., 2016. A combined assessment of air and noise pollution on the high line, New York City. Transport. Res. Transport Environ. 42, 91–103.

Klingberg, J., Broberg, M., Strandberg, B., Thorsson, P., Pleijel, H., 2017. Influence of urban vegetation on air pollution and noise exposure – A case study in Gothenburg, Sweden. Sci. Total Environ. 599–600, 1728–1739.

Kumar, P., Morawska, L., Martani, C., Biskos, G., Neophytou, M., Di Sabatino, S., Bell, M., Norford, L., Britter, R., 2015. The rise of low-cost sensing for managing air pollution in cities. Environ. Int. 75, 199–205.

Kurppa, M., Hellsten, A., Auvinen, M., Raasch, S., Vesala, T., Järvi, L., 2018. Ventilation and air quality in city blocks using large-eddy simulation – Urban planning perspective. Atmosphere 9, 65.

Li, X.L., Wang, J.S., Tu, X.D., Liu, W., Huang, Z., 2007. Vertical variations of particle number concentration and size distribution in a street canyon in Shanghai, China. Sci. Total Environ. 378 (3), 306–316.

Li, J., Fu, Q., Huo, J., Wang, D., Yang, W., Bian, Q., Duan, Y., Zhang, Y., Pan, J., Lin, Y., Huang, K., Bai, Z., Wang, S.-H., Fu, J.S., Louie, P.K.K., 2015. Tethered balloon-based black carbon profiles within the lower troposphere of Shanghai in the 2013 East China smog. Atmos. Environ. 123, 327–338.

Li, X.-B., Wang, D., Lu, Q.-C., Peng, Z.-R., Fu, Q., Hu, X.-M., Huo, J., Xiu, G., Li, B., Li, C., Wang, D.-S., Wang, H., 2018. Three-dimensional analysis of ozone and $PM_{2.5}$ distributions obtained by observations of tethered balloon and unmanned aerial vehicle in Shanghai, China. Stoch. Environ. Res. Risk Assess. 32 (5), 1189–1203.

Mamali, D., Marinou, E., Sciare, J., Pikridas, M., Kokkalis, P., Kottas, M., Binietoglou, I., Tsekeri, A., Keleshis, C., Engelmann, R., Baars, H., Ansmann, A., Amiridis, V., Russchenberg, H., Biskos, G., 2018. Vertical profiles of aerosol mass concentration derived by unmanned airborne in situ and remote sensing instruments during dust events. Atmos. Meas. Tech. 11 (5), 2897–2910.

Maronga, B., Banzhaf, S., Burmeister, C., Esch, T., Forkel, R., Fröhlich, D., Fuka, V., Gehrke, K.F., Geletič, J., Giersch, S., Gronemeier, T., Groß, G., Heldens, W., Hellsten, A., Hoffmann, F., Inagaki, A., Kadasch, E., Kanani-Sühring, F., Ketelsen, K., Khan, B.A., Knigge, C., Knoop, H., Krč, P., Kurppa, M., Maamari, H., Matzarakis, A., Mauder, M., Pallasch, M., Pavlik, D., Pfafferott, J., Resler, J., Rissmann, S., Russo, E., Salim, M., Schrempf, M., Schwenkel, J., Seckmeyer, G., Schubert, S., Sühring, M., von Tils, R., Vollmer, L., Ward, S., Witha, B., Wurps, H., Zeidler, J., Raasch, S., 2020. Overview of the palm model system 6.0. Geosci. Model Dev. (GMD) 13, 1335–1373.

Maronga, B., Winkler, M., Li, D., 2022. Can areawide building retrofitting affect the urban microclimate? An LES study for Berlin, Germany. J. Appl. Meteorol. Climatol. 61, 800–817.

Martinuzzi, R., Tropea, C., 1993. The flow around a surface-mounted, prismatic obstacle placed in a fully developed channel flow. J. Fluids Eng. - Transac. ASME 115, 85–92.

Mead, M.I., Popoola, O.A.M., Stewart, G.B., Landshoff, P., Calleja, M., Hayes, M., Baldovi, J.J., McLeod, M.W., Hodgson, T.F., Dicks, J., Lewis, A., Cohen, J., Baron, R., Saffell, J.R., Jones, R.L., 2013. The use of electrochemical sensors for monitoring urban air quality in low-cost, high-density networks. Atmos. Environ. 70, 186–203.

Micallef, A., Deuchar, C.N., Colls, J.J., 1998a. Indoor and outdoor measurements of vertical concentration profiles of airborne particulate matter. Sci. Total Environ. 215 (3), 209–216.

Micallef, A., Caldwell, J., Colls, J.J., 1998b. The influence of human activity on the vertical distribution of airborne particle concentration in confined environments: preliminary results. Indoor Air 8 (2), 131–136. https://onlinelibrary.wiley.com/doi/pdf/10.1111/j.1600-0668.1998.t01-1-00008.x.

Micallef, A., Deuchar, C.N., Colls, J.J., 1998c. Indoor and outdoor measurements of vertical concentration profiles of airborne particulate matter. Sci. Total Environ. 215 (3), 209–216.

Micallef, A., Colls, J.J., Caldwell, J., 1999. Measurement of vertical concentration profiles of airborne particulate matter in indoor environments: Implications for refinement of models and monitoring campaigns. Int. J. Environ. Health Res. 9 (1), 5–18.

Morawska, L., Thai, P.K., Liu, X., Asumadu-Sakyi, A., Ayoko, G., Bartonova, A., Bedini, A., Chai, F., Christensen, B., Dunbabin, M., Gao, J., Hagler, G.S.W., Jayaratne, R., Kumar, P., Lau, A.K.H., Louie, P.K.K., Mazaheri, M., Ning, Z., Motta, N., Mullins, B., Rahman, M., Ristovski, Z., Shafiei, M., Tjondronegoro, D., Westerdahl, D., Williams, R., 2018. Applications of low-cost sensing technologies for air quality monitoring and exposure assessment: how far have they gone? Environ. Int. 116, 286–299.

Moreau-Guigon, E., Motelay-Massei, A., Harner, T., Pozo, K., Diamond, M., Chevreuil, M., Blanchoud, H., 2007. Vertical and temporal distribution of persistent organic pollutants in Toronto. 1. Organochlorine pesticides. Environ. Sci. Technol. 41 (7), 2172–2177.

Nagendra, S.M.S., Yasa, P.R., Narayana, M.V., Khadirnaikar, S., Rani, P., 2019. Mobile monitoring of air pollution using low cost sensors to visualize spatio-temporal variation of pollutants at urban hotspots. Sustain. Cities Soc. 44, 520–535.

Pearce, J.L., Beringer, J., Nicholls, N., Hyndman, R.J., Tapper, N.J., 2011. Quantifying the influence of local meteorology on air quality using generalized additive models. Atmos. Environ. 45 (6), 1328–1336.

Petäj, T., Ovaska, A., Fung, P.L., Poutanen, P., Yli-Ojanperä, J., Suikkola, J., Laakso, M., Mäkelä, T., Niemi, J.V., Keskinen, J., Järvinen, A., Kuula, J., Mona, K., Hussein, T., Tarkoma, S., Kulmala, M., Karppinen, A., Manninen, H.E., Timonen, H., 2021. Added value of vaisala AQT530 sensors as a part of a sensor network for comprehensive air quality monitoring. Front. Environ. Sci. 9.

Pirintsos, S.A., Matsi, T., Vokou, D., Gaggi, C., Loppi, S., 2006. Vertical distribution patterns of trace elements in an urban environment as reflected by their accumulation in lichen transplants. J. Atmos. Chem. 54 (2), 121–131.

Qiu, Y., Tao, S., Yun, X., Du, W., Shen, G., Lu, C., Yu, X., Cheng, H., Ma, J., Xue, B., Tao, J., Dai, J., Ge, Q., 2019. Indoor $PM_{2.5}$ profiling with a novel side-scatter indoor lidar. Environ. Sci. Technol. Lett. 6 (10), 612–616.

R Core Team, 2017. R: A Language and Environment for Statistical Computing. R Foundation for Statistical Computing. Eprint: https://www.R-project.org/. Last accessed: 17 October 2023.

Redmon, J., Farhadi, A., 2018. YOLOv3: An Incremental Improvement. Cornell University. Eprint: https://doi.org/10.48550/arXiv.1804.02767. Last accessed: 25 October 2023.

Renard, J.-B., Michoud, V., Giacomoni, J., 2020. Vertical profiles of pollution particle concentrations in the boundary layer above Paris (France) from the optical aerosol counter LOAC onboard a touristic balloon. Sensors 20 (4), 1111.

Resler, J., Eben, K., Geletič, J., Krč, P., Rosecký, M., Sühring, M., Belda, M., Fuka, V., Halenka, T., Huszár, P., Karlický, J., Benešová, N., Ďoubalová, J., Honzáková, K., Keder, J., Nápravníková, Š., Vlček, O., 2021. Validation of the palm model system 6.0 in a real urban environment: A case study in Dejvice, Prague, the Czech Republic. Geosci. Model Dev. (GMD) 14, 4797–4842.

Rogulski, M., Badyda, A., Gayer, A., Reis, J., 2022. Improving the quality of measurements made by Alphasense NO_2 non-reference sensors using the mathematical methods. Sensors 22 (10), 3619.

Ross, Z., Kheirbek, I., Clougherty, J.E., Ito, K., Matte, T., Markowitz, S., Eisl, H., 2011. Noise, air pollutants and traffic: continuous measurement and correlation at a high-traffic location in New York City. Environ. Res. 111 (8), 1054–1063.

Russell, H.S., Frederickson, L.B., Kwiatkowski, S., Emygdio, A.P., Kumar, P., Schmidt, J. A., Hertel, O., Johnson, M.S., 2022. Enhanced ambient sensing environment – A new method for calibrating low-cost gas sensors. Sensors 22, 7238.

Schmitz, S., Villena, G., Caseiro, A., Meier, F., Kerschbaumer, A., von Schneidemesser, E., 2023. Calibrating low-cost sensors to measure vertical and horizontal gradients of NO_2 and O_3 pollution in three street canyons in berlin. Atmos. Environ., 119830

Sensirion, 2020. Datasheet SPS30. Particulate matter sensor for air quality monitoring and control. https://www.datasheetbank.com/datasheet-download/98164 1/1/SENSIRION/SPS30. (Accessed 25 November 2022). Data Sheet.

Shen, L., Cheng, Y., Bai, X., Dai, H., Wei, X., Sun, L., Yang, Y., Zhang, J., Feng, Y., Jie Li, Y., Chen, D.-R., Liu, J., Gui, H., 2022. Vertical profile of aerosol number size distribution during a haze pollution episode in Hefei, China. Sci. Total Environ. 814, 152693.

Shi, Y., Wang, D., Huo, J., Duan, Y., Lin, Y., Huang, K., Fu, Q., Xiu, G., 2022. Vertically-resolved sources and secondary formation of fine particles: A high resolution tethered mega-balloon study over Shanghai. Sci. Total Environ. 802, 149681.

Shu, S., Yang, P., Zhu, Y., 2014. Correlation of noise levels and particulate matter concentrations near two major freeways in Los Angeles, California. Environ. Pollut. 193, 130–137.

Song, R.-F., Wang, D.-S., Li, X.-B., Li, B., Peng, Z.-R., He, H.-D., 2021. Characterizing vertical distribution patterns of $PM_{2.5}$ in low troposphere of Shanghai city, China: Implications from the perspective of unmanned aerial vehicle observations. Atmos. Environ. 265, 118724.

Tenailleau, Q.M., Bernard, N., Pujol, S., Parmentier, A.-L., Boilleaut, M., Houot, H., Joly, D., Mauny, F., 2016. Do outdoor environmental noise and atmospheric NO_2 levels spatially overlap in urban areas? Environ. Pollut. 214, 767–775.

Tétreault, L.-F., Perron, S., Smargiassi, A., 2013. Cardiovascular health, traffic-related air pollution and noise: are associations mutually confounded? A systematic review. Int. J. Publ. Health 58 (5), 649–666.

Tevlin, A.G., Li, Y., Collett, J.L., McDuffie, E.E., Fischer, E.V., Murphy, J.G., 2017. Tall tower vertical profiles and diurnal trends of ammonia in the Colorado front range. J. Geophys. Res. Atmos. 122 (22), 468–12,487.

Tryner, J., Mehaffy, J., Miller-Lionberg, D., Volckens, J., 2020. Effects of aerosol type and simulated aging on performance of low-cost PM sensors. J. Aerosol Sci. 150, 105654.

United Nations, 2018. Revision of World Urbanization Prospects, 2023-05-15. Eprint: https://www.un.org/en/desa/2018-revision-world-urbanization-prospects. Last accessed: 25 October 2023.

Väkevä, M., Hämeri, K., Kulmala, M., Lahdes, R., Ruuskanen, J., Laitinen, T., 1999. Street level versus rooftop concentrations of submicron aerosol particles and gaseous pollutants in an urban street canyon. Atmos. Environ. 33 (9), 1385–1397.

Vardoulakis, S., Gonzalez-Flesca, N., Fisher, B.E.A., 2002. Assessment of traffic-related air pollution in two street canyons in Paris: implications for exposure studies. Atmos. Environ. 36 (6), 1025–1039.

Wang, D., Wang, Z., Peng, Z.-R., Wang, D., 2020. Using unmanned aerial vehicle to investigate the vertical distribution of fine particulate matter. Int. J. Environ. Sci. Technol. 17 (1), 219–230.

Wang, D., Huo, J., Duan, Y., Zhang, K., Ding, A., Fu, Q., Luo, J., Fei, D., Xiu, G., Huang, K., 2021. Vertical distribution and transport of air pollutants during a regional haze event in eastern China: a tethered mega-balloon observation study. Atmos. Environ. 246, 118039.

Weber, S., 2009. Spatio-temporal covariation of urban particle number concentration and ambient noise. Atmos. Environ. 43 (34), 5518–5525.

Wei, P., Ning, Z., Ye, S., Sun, L., Yang, F., Wong, K.C., Westerdahl, D., Louie, P.K.K., 2018. Impact analysis of temperature and humidity conditions on electrochemical sensor response in ambient air quality monitoring. Sensors 18 (2), 59.

Winderlich, J., Gerbig, C., Kolle, O., Heimann, M., 2014. Inferences from CO_2 and CH_4 concentration profiles at the Zotino Tall Tower Observatory (ZOTTO) on regional summertime ecosystem fluxes. Biogeosciences 11 (7), 2055–2068.

Wong, P.P.Y., Lai, P.-C., Allen, R., Cheng, W., Lee, M., Tsui, A., Tang, R., Thach, T.-Q., Tian, L., Brauer, M., Barratt, B., 2019. Vertical monitoring of traffic-related air pollution (TRAP) in urban street canyons of Hong Kong. Sci. Total Environ. 670, 696–703.

Wood, S., Scheipl, F., 2020. gamm4: Generalized Additive Mixed Models Using 'mgcv' and 'lme4'. https://CRAN.R-project.org/package=gamm4. (Accessed 1 November 2022).

Wu, C.-D., MacNaughton, P., Melly, S., Lane, K., Adamkiewicz, G., Durant, J.L., Brugge, D., Spengler, J.D., 2014. Mapping the vertical distribution of population and particulate air pollution in a near-highway urban neighborhood: implications for exposure assessment. J. Expo. Sci. Environ. Epidemiol. 24 (3), 297–304.

Xie, Z.T., Castro, I.P., 2009. Large-eddy simulation for flow and dispersion in urban streets. Atmos. Environ. 43, 2174–2185.

Xing, C., Liu, C., Wang, S., Chan, K.L., Gao, Y., Huang, X., Su, W., Zhang, C., Dong, Y., Fan, G., Zhang, T., Chen, Z., Hu, Q., Su, H., Xie, Z., Liu, J., 2017. Observations of the vertical distributions of summertime atmospheric pollutants and the corresponding ozone production in Shanghai, China. Atmos. Chem. Phys. 17 (23), 14275–14289.

Zhang, X., Chen, X., Zhang, X., 2018. The impact of exposure to air pollution on cognitive performance. Proc. Natl. Acad. Sci. USA 115 (37), 9193–9197.

Zhang, J., Wei, Y., Fang, Z., 2019a. Ozone pollution: a major health hazard worldwide. Front. Immunol. 10.

Zhang, K., Zhou, L., Fu, Q., Yan, Lei, Bian, Q., Wang, D., Xiu, G., 2019b. Vertical distribution of ozone over Shanghai during late spring: a balloon-borne observation. Atmos. Environ. 208, 48–60.

Zheng, T., Li, B., Li, X.-B., Wang, Z., Li, S.-Y., Peng, Z.-R., 2021. Vertical and horizontal distributions of traffic-related pollutants beside an urban arterial road based on unmanned aerial vehicle observations. Build. Environ. 187, 107401.

Zheng, S., Shen, H., Shen, G., Chen, Y., Ma, J., Cheng, H., Tao, S., 2022. Vertically-resolved indoor measurements of air pollution during Chinese cooking. Environ. Sci. Ecotechnol. 12, 100200.